RESEARCH ARTICLE | SEPTEMBER 25 2024

A numerical model for solitary wave breaking based on the phase-field lattice Boltzmann method

Jiahe Zhou (周嘉禾) ; Qinghe Zhang (张庆河) ; Guangwei Liu (刘光威) ; Jinfeng Zhang (张金凤) ; Enbo Xing (邢恩博)

Physics of Fluids 36, 092125 (2024)
https://doi.org/10.1063/5.0224015

Physics of Fluids ARTICLE pubs.aip.org/aip/pof

A numerical model for solitary wave breaking based on the phase-field lattice Boltzmann method

Cite as: Phys. Fluids **36**, 092125 (2024); doi: 10.1063/5.0224015
Submitted: 18 June 2024 · Accepted: 30 August 2024 ·
Published Online: 25 September 2024

Jiahe Zhou (周嘉禾),[1] Qinghe Zhang (张庆河),[1] Guangwei Liu (刘光威),[1,a)] Jinfeng Zhang (张金凤),[1,2] and Enbo Xing (邢恩博)[1]

AFFILIATIONS

[1]State Key Laboratory of Hydraulic Engineering Intelligent Construction and Operation, Tianjin University, Tianjin 300072, China
[2]Key Laboratory of Earthquake Engineering Simulation and Seismic Resilience of China Earthquake Administration, Tianjin University, Tianjin 300350, China

[a)]Author to whom correspondence should be addressed: guangweiliu@tju.edu.cn

ABSTRACT

This study presents a numerical investigation of a solitary wave breaking over a slope by using the phase-field lattice Boltzmann method. The incompressible two-phase flow equations are solved by using a velocity-based formulation of the two-phase lattice Boltzmann method with a central-moment collision model to accurately simulate wave breaking problems. For interface capture, a phase-field lattice Boltzmann method that ensures mass conservation is employed. The validity of the proposed method is confirmed through solitary wave propagation and transformation problems, and the obtained results are in good agreement with the experimental and calculated results. The proposed method is then employed to analyze wave breaking on a slope, demonstrating strong concordance with experimental data and existing computational findings. By analyzing the instantaneous flow characteristics and the temporal evolution of the variation in kinetic, potential, and total energy from deep to shallow water, the model can reveal the macroscopic characteristics of solitary wave breaking. Because the phase-field model effectively simulates wave breaking and air entrainment, it can depict wave energy dissipation more accurately than the single-phase lattice Boltzmann method with free surface tracking.

I. INTRODUCTION

Wave breaking is a common phenomenon in nearshore areas. Understanding the mechanism of wave breaking is essential for comprehending the transfer of kinetic energy, energy dissipation, and other wave dynamic characteristics and is significant for further studying wave–structure interactions and nearshore sediment transport. As an example of extreme waves, solitary waves are widely used to represent tsunamis and long nearshore waves. Therefore, many studies, including experimental,[1–8] theoretical and numerical investigations,[9–24] have been carried out to investigate the breaking of solitary waves.

Among studies of different methods, numerical simulation, due to its ability to reveal the fluid motion details of solitary wave breaking, has rapidly increased in popularity in recent years. Most numerical models with grids apply free surface tracking methods, such as the marker-and-cell (MAC) method,[25,26] level-set method,[27] and volume-of-fluid (VOF) method,[28,29] to capture violent water surface deformation in solitary wave breaking. Additionally, the smoothed particle hydrodynamics (SPH) method has been increasingly applied to investigate solitary wave breaking due to its ability to handle violent free surface motion.[30–33] However, the SPH method uses particles in the simulation, which is computationally costly as particle sizes decrease. Especially wave breaking, the variation in the spatial distribution of water particles impacts the computational expense of every partition, leading to a notable breakdown in parallel scalability.[34]

For the creation of a high-performance numerical wave model, we utilize the lattice Boltzmann method (LBM). The LBM can be regarded as a kind of Euler method, which is a numerical method for solving the Boltzmann equation on discrete lattice points with special space–time and velocity discretization.[35] As all operations require only local neighborhood information,[36] the LBM has high computational efficiency and parallel scalability.[37] Recently, numerous numerical studies have been conducted on the propagation and breaking of solitary waves using the LBM.[38–41] However, these studies are using single-phase flow models, neglecting the influence of air movement

over the free water surface and the density difference between water and air. In fact, the role of air during wave breaking is significant, and the droplets/bubbles of different sizes enhance the energy dissipation during the wave breaking.[44,45] Therefore, the development of a two-phase LBM model is essential for simulating solitary wave breaking to consider the interaction between air and water.

The objective of the present paper is to develop a phase-field lattice Boltzmann model (PFLBM) for air–water two-phase flows to simulate the breaking of solitary waves. Unlike the VOF[42] and level-set[27] schemes, which solve advection-type equations, phase-field models solve the advection–diffusion equation, which can be expressed directly by a standard lattice Boltzmann equation (LBE) with additional force terms.[46] This not only simplifies the implementation of the model and improves the computational efficiency, but also makes the model more suitable for parallel implementation.

This paper is organized as follows. In Sec. II, the governing equations and lattice Boltzmann equations for two-phase flows are described. In Sec. III, the proper grid size, time step, and interface thickness are chosen through sensitivity analysis. In Sec. IV, the proposed method is validated through theoretical solutions and experimental results, with the simulation results compared to SPH results to evaluate the accuracy of interface capture. Section V simulates three typical solitary wave breaking phenomena, analyzing the differences in breaking positions and air entrainment among various breaker types, as well as the instantaneous flow characteristics of breaking waves. It then compares single-phase and two-phase LBM simulations by evaluating the evolution of kinetic, potential, and total energy during wave breaking, and investigates the effects of kinetic energy transfer between water and air on energy dissipation. In Sec. VI, concluding remarks are given.

II. NUMERICAL METHODS

The present model uses the LBM to solve the Navier–Stoke (N–S) equations and combines the phase-field method to track the motion of solitary waves. The flowchart of the model is shown in Fig. 1. The introduction and implementation of the numerical model are described in Subsections II A–II D, including the governing equations and the corresponding LB equations and their solution, the boundary conditions, and the implementation of the algorithm.

A. Phase-field lattice Boltzmann method for interface tracking

1. Interface tracking equation

The interface-tracking equation in this study is built upon the Allen–Cahn equation.[46] In this model, the phase parameters of different fluids are expressed by the phase field ϕ. $\phi_L = 0$ and $\phi_H = 1$ are the phase field value of the light and heavy fluids, respectively. The phase-field equation governs the evolution of the interface between the two fluids,[49]

$$\frac{\partial \phi}{\partial t} + \nabla \cdot \phi \mathbf{u} = \nabla \cdot M \left[\left(\nabla \phi - \frac{\nabla \phi}{|\nabla \phi|} \frac{\left[1 - 4(\phi - \phi_0)^2\right]}{\xi} \right) \right], \quad (1)$$

where t is the time, $\mathbf{u}$ is the macroscopic velocity vector, M is the mobility, ξ is the interfacial thickness, and $\phi_0 = 0.5$ indicates the location of the interface. The initialization of the phase field for an interface located at η of the solitary wave is assumed to vary according to

$$\phi(x, y) = \phi_0 - \frac{\phi_H - \phi_L}{2} \tanh\left(\frac{y - interface}{\xi/2} \right), \quad (2)$$

$$interface(x, t) = SWL + \eta(x, t), \quad (3)$$

where $interface(x, t)$ is the location of the interface, SWL is the still water level, and $\eta(x, t)$ is the water level expression.

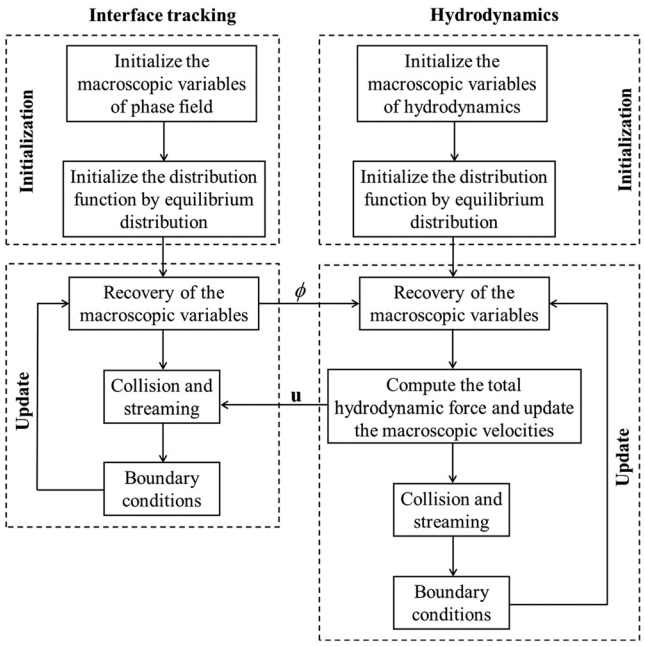

FIG. 1. Flowchart of the interface tracking and hydrodynamics in the present model.

2. LBE for interface tracking

In LBM, instead of solving the intended equations directly, the corresponding lattice Boltzmann equation is solved. Based on the above governing equation [Eq. (1)], we adopt the following LBE for tracking the interface between different fluids in the central moment (CM) space, which is split into collision and streaming steps:

$$h_a^*(\mathbf{x}, t) = \tilde{h}_\alpha(\mathbf{x}, t) - \mathbb{S}^\phi \left(\tilde{h}_\alpha(\mathbf{x}, t) - \tilde{h}_\alpha^{eq}(\mathbf{x}, t) \right) + (1 - \mathbb{S}^\phi/2)\tilde{\mathbf{F}}_\alpha^\phi(\mathbf{x}, t), \quad (4)$$

$$h_\alpha(\mathbf{x} + e_\alpha \delta t, t + \delta t) = \mathbb{M}^{-1}\mathbb{N}^{-1} h_a^*(\mathbf{x}, t), \quad (5)$$

where h_α is the α-th distribution function for the phase field and the superscript $(\sim)$ represents the distribution function in the central moment space. $\mathbb{M}$ and $\mathbb{N}$ are the transformation matrix and shift matrix in the central moment space, respectively. The relaxation matrices $\mathbb{S}^\phi$ have a diagonal form specified as[47]

$$\mathbb{S}^\phi = diag\left(\left[s_0^\phi, s_M^\phi, s_M^\phi, s_2^\phi, s_2^\phi, s_2^\phi, s_3^\phi, s_3^\phi, s_4^\phi \right] \right). \quad (6)$$

The relaxation frequencies are specified as follows:

$$s_M^\phi = \frac{1}{\tau_M} = \frac{1}{\tau_\phi + \frac{1}{2}}, \tag{7}$$

while the rest is conserved by setting the relaxation frequencies to a unit,[47] $s_1^\phi = s_2^\phi = s_3^\phi = s_4^\phi = 1$, and $\tau_\phi = M/c_s^2$ is the phase-field relaxation time.

The central moments of force vectors $\tilde{\mathbf{F}}^\phi$ are given by

$$\tilde{\mathbf{F}}^\phi = \left[0, F_x/\rho, F_y/\rho, 0, 0, 0, c_s^2 F_y^\phi, c_s^2 F_x^\phi, 0\right]. \tag{8}$$

We define the total hydrodynamic force as $\mathbf{F} = (F_x, F_y)$, and the forcing term for the phase field $\mathbf{F}^\phi$ is given by

$$\mathbf{F}^\phi(x,t) = \delta t \frac{\left[1 - 4(\phi - \phi_0)^2\right]}{\xi} c_s^2 \cdot \mathbf{n}, \tag{9}$$

where $c_s = c/\sqrt{3}$ is the speed of sound in the system, and the normal vector $\mathbf{n}$ is calculated as follows:

$$\mathbf{n} = \frac{\nabla\phi}{|\nabla\phi| + \varepsilon}, \tag{10}$$

where $\varepsilon = 10^{-12}$ is a small number to prevent the denominator from being zero.

The gradient of the phase field is

$$\nabla\phi = \frac{c}{c_s^2 \delta x} \sum_\alpha \mathbf{e}_\alpha \omega_\alpha \phi(\mathbf{x} + \mathbf{e}_\alpha \delta t, t), \tag{11}$$

$$|\nabla\phi| = \sqrt{\phi_x^2 + \phi_y^2}, \tag{12}$$

where ω_α and $\mathbf{e}_\alpha$ are the weight coefficients and the mesoscopic velocity set, respectively.

The equilibrium phase-field distribution function of the raw moments is defined as[46]

$$h_\alpha^{eq} = \phi\omega_\alpha \left[1 + \frac{\mathbf{e}_\alpha \cdot \mathbf{u}}{c_s^2} + \frac{(\mathbf{e}_\alpha \cdot \mathbf{u})^2}{2c_s^4} - \frac{\mathbf{u} \cdot \mathbf{u}}{2c_s^2}\right]. \tag{13}$$

The equilibrium phase-field distribution function in the central moment space $\tilde{h}_\alpha^{eq}$ is defined as[47]

$$\tilde{h}^{eq} = \left[k_{00}^\phi, 0, 0, c_s^2 k_{00}^\phi, 0, 0, 0, c_s^4 k_{00}^\phi\right]^T, \tag{14}$$

where $k_{00}^\phi = \phi$ is the zeroth-order moments of the phase-field distribution function corresponding to the value of the phase field.

After solving the LBE in Eqs. (4) and (5) using a routine collision-streaming sequence, the value of the phase field ϕ is updated independently according to

$$\phi^{n+1} = \sum_\alpha h_\alpha. \tag{15}$$

B. Phase-field lattice Boltzmann method for hydrodynamics

1. Navier-Stokes equations

The continuity and momentum equations for incompressible two-phase flows are given by

$$\frac{\partial\rho}{\partial t} + \nabla \cdot \rho\mathbf{u} = 0, \tag{16}$$

$$\rho\left(\frac{\partial\mathbf{u}}{\partial t} + \mathbf{u} \cdot \nabla\mathbf{u}\right) = -\nabla p + \nabla \cdot \left(\mu[\nabla\mathbf{u} + \nabla^T\mathbf{u}]\right) + \mathbf{F}_b, \tag{17}$$

where ρ is the density, $\mathbf{u} = (u_x, u_y)$ is the velocity, p is the pressure, μ is the dynamic viscosity, $\mathbf{F}_b$ is the body force, and t is the time. A mixed-phase fluid approach is employed, where the density and viscosity are defined as follows:

$$\rho = \rho_L + \phi(\rho_H - \rho_L), \tag{18}$$

$$\mu = \mu_L + \phi(\mu_H - \mu_L), \tag{19}$$

where ρ_L and ρ_H are the densities of the light and heavy fluids, respectively, and this simulation is performed with the densities of water and air set to $\rho_L = 0.001$ lu (lattice unit) and $\rho_H = 1$ lu, respectively.

2. LBE for hydrodynamics

Based on Eqs. (16) and (17), the LBE for hydrodynamics is defined as[46]

$$g_\alpha^*(\mathbf{x},t) = \tilde{g}_\alpha(\mathbf{x},t) + \tilde{\Omega}_\alpha(\mathbf{x},t) + (1 - \mathbb{S}^\phi/2)\tilde{F}_\alpha(\mathbf{x},t), \tag{20}$$

$$g_\alpha(\mathbf{x} + e_\alpha\delta t, t + \delta t) = \mathbb{M}^{-1}\mathbb{N}^{-1} g_\alpha^*(\mathbf{x},t), \tag{21}$$

where g_α is the α-th distribution function for the velocity field and the superscript $(\sim)$ represents the distribution function in the central moment space.

The collision in the central moment space $\tilde{\Omega}_\alpha(\mathbf{x},t)$ is defined as

$$\tilde{\Omega}_\alpha(\mathbf{x},t) = \mathbb{S} \cdot \left(\tilde{g}_\alpha^{eq}(\mathbf{x},t) - \tilde{g}_\alpha(\mathbf{x},t)\right), \tag{22}$$

where $\tilde{g}_\alpha^{eq}$ is the α-th equilibrium distribution function in central moment space for the velocity field.[44]

The diagonal form of the relaxation matrices $\mathbb{S}$ is defined by the following formula:[47]

$$\mathbb{S} = diag\left([s_0, s_1, s_1], \begin{bmatrix} s_+ & s_- \\ s_- & s_+ \end{bmatrix}, [s_v, s_3, s_3, s_4]\right), \tag{23}$$

where $s_+ = (s_b + s_v)/2$, $s_- = (s_b - s_v)/2$, and the corresponding relaxation frequencies, s_b and s_v, can be determined by the bulk and kinematic viscosities,

$$s_b = \frac{1}{\tau_b} = \frac{1}{\frac{\zeta}{c_s^2\delta t} + \frac{1}{2}}, \tag{24}$$

$$s_v = \frac{1}{\tau} = \frac{1}{\frac{\nu}{c_s^2\delta t} + \frac{1}{2}}, \tag{25}$$

where ζ is the bulk viscosity, the bulk relaxation rate is specified as $s_b = 1$,[47] and relaxation constants are set to unity, $s_0 = s_1 = s_2 = s_3 = s_4 = 1$.

The equilibrium hydrodynamic distribution function in the raw moment space and central moment space, g_α^{eq} and $\tilde{g}_\alpha^{eq}$, are defined as[46,47]

$$g_\alpha^{eq} = p^*\omega_\alpha + \omega_\alpha \left[\frac{\mathbf{e}_\alpha \cdot \mathbf{u}}{c_s^2} + \frac{(\mathbf{e}_\alpha \cdot \mathbf{u})^2}{2c_s^4} - \frac{\mathbf{u} \cdot \mathbf{u}}{2c_s^2}\right], \tag{26}$$

$$\tilde{g}_{\alpha}^{eq} = \begin{bmatrix} k_{00} \\ (k_{00}-1)(-u_x) \\ (k_{00}-1)(-u_y) \\ (k_{00}-1)(u_x^2+c_s^2)+c_s^2 \\ (k_{00}-1)(u_y^2+c_s^2)+c_s^2 \\ (k_{00}-1)u_x u_y \\ (k_{00}-1)(-u_y)(u_x^2+c_s^2) \\ (k_{00}-1)(-u_x)(u_y^2+c_s^2) \\ (k_{00}-1)(u_x^2u_y^2+c_s^2(u_x^2+u_y^2)+c_s^4)+c_s^4 \end{bmatrix}, \quad (27)$$

where k_{00} is the raw, zeroth order moments of the hydrodynamic distribution function corresponding to the values of the normalized pressure $p^* = p/(\rho c_s^2)$.

The components of the force vectors in the central moment space $\tilde{\mathbf{F}}$ are

$$\tilde{\mathbf{F}} = \left[0, F_x/\rho, F_y/\rho, 0, 0, 0, c_s^2 F_y/\rho, c_s^2 F_x/\rho, 0\right], \quad (28)$$

and the total hydrodynamic force $\mathbf{F} = (F_x, F_y)$ is

$$\mathbf{F} = \mathbf{F}_b + \mathbf{F}_p + \mathbf{F}_\mu, \quad (29)$$

where $\mathbf{F}_b$ is the body force, $\mathbf{F}_p$ is the pressure force, and $\mathbf{F}_\mu$ is the viscous force. The surface tension is omitted because it is insignificant compared to the body force, pressure force, and viscous force for solitary waves.

The body force is

$$\mathbf{F}_b = -\rho \mathbf{g}. \quad (30)$$

The pressure force can be written as

$$\mathbf{F}_p = -p^* c_s^2 \nabla \rho. \quad (31)$$

The density gradient $\nabla\rho$ can be replaced with the phase field gradient using $\nabla\rho = (\rho_H - \rho_L)\nabla\phi$.

The viscous force is

$$\mathbf{F}_\mu = \nu\left[\nabla \mathbf{u} + (\nabla \mathbf{u})^T\right] \cdot \nabla \rho, \quad (32)$$

where ν is the kinematic viscosity, and it is related to the relaxation time τ by

$$\nu = \tau c_s^2 \delta t. \quad (33)$$

The relaxation time is calculated from the phase field by using linear interpolation

$$\tau = \tau_L + (\phi - \phi_L)(\tau_H - \tau_L). \quad (34)$$

The initialization of the relaxation time of light and heavy fluids τ_L and τ_H is related to the kinematic viscosity,

$$\begin{cases} \tau_L = \dfrac{\nu_L}{c_s^2 \delta t}, \\ \tau_H = \dfrac{\nu_H}{c_s^2 \delta t}, \end{cases} \quad (35)$$

while for the CM model

$$\begin{aligned} F_{\mu,i}^{CM} &= -\frac{\nu}{c_s^2 \delta t}\left[\sum_\beta e_{\beta i} e_{\beta j} \times \sum_\alpha (\mathbb{M}^{-1}\mathbb{N}^{-1}\mathbb{S})_{\beta\alpha}(\tilde{g}_\alpha - \tilde{g}_\alpha^{eq})\right]\frac{\partial \rho}{\partial x_j} \\ &= -\tau\left[\sum_\beta e_{\beta i} e_{\beta j} \times \sum_\alpha (\mathbb{M}^{-1}\mathbb{N}^{-1}\mathbb{S})_{\beta\alpha}(\tilde{g}_\alpha - \tilde{g}_\alpha^{eq})\right] \\ &\quad \times (\rho_H - \rho_L)\frac{\partial \phi}{\partial x_j}. \end{aligned} \quad (36)$$

After solving the LBE in Eqs. (20) and (21) using a routine collision-streaming sequence, the normalized pressure $p^* = p/(\rho c_s^2)$ is updated independently according to

$$p^{*n+1} = \sum_\alpha g_\alpha. \quad (37)$$

The macroscopic velocity is updated semi-implicitly

$$\mathbf{u}^{n+1} = \sum_\alpha g_\alpha \mathbf{e}_\alpha + \frac{1}{2}\frac{\mathbf{F}}{\rho}\delta t. \quad (38)$$

C. Boundary conditions

Different from the macroscopic fluid dynamics models, LBM only solves the distribution function, so the boundary conditions of LBM are a kind of numerical format in which the distribution function is reconstructed according to the macroscopic quantity. The introduction of the boundary conditions is described in Subsections II C 1 and II C 2.

1. Free-slip boundary conditions

For the distribution functions of hydrodynamics, the specular reflection scheme is applied,

$$g_{2,5,6}(\mathbf{x}, t) = g_{4,8,7}(\mathbf{x}, t). \quad (39)$$

To ensure the conservation of mass on the boundary, the unknown phase-field distribution function is determined by bounce-back scheme

$$h_{2,5,6}(\mathbf{x}, t) = h_{4,7,8}(\mathbf{x}, t). \quad (40)$$

2. Cyclic boundary conditions

The physical quantities of the flow on both sides of the cyclic boundaries are the same, and the material flowing out of one boundary flows in from the other boundary. In these two cyclic boundaries, the grid point of one boundary is replaced by the internal grid point at the corresponding position of the other boundary to achieve the infinite extension of the calculation domain in the specified direction.

D. Algorithm of computation

The algorithm for computation shown in Fig. 2 is summarized as follows:

- **Step 1:** Initialize the macroscopic variables: phase-field variable [Eqs. (2) and (3)], phase-field gradient $\nabla\phi$ [Eq. (11)], density ρ [Eq. (18)], viscosity μ [Eq. (19)], pressure $p(\mathbf{x}, 0)$, and macroscopic velocity $\mathbf{u}(\mathbf{x}, 0)$.
- **Step 2:** Initialize the distribution functions: $g(\mathbf{x}, 0)$ for the hydrodynamic distribution function [Eq. (13)] and $h(\mathbf{x}, 0)$ for the phase-field distribution function [Eq. (26)].

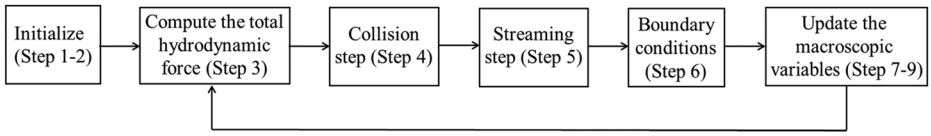

FIG. 2. Computation algorithm.

- **Step 3:** Compute the total hydrodynamic force: $\mathbf{F} = (F_x, F_y)$ [Eqs. (30)–(36)].
- **Step 4:** Compute the post-collision distribution functions: $h_\alpha * (\mathbf{x}, t)$ [Eq. (4)] and $g_\alpha * (\mathbf{x}, t)$ [Eq. (20)].
- **Step 5:** Update the distribution functions (streaming steps): $h_\alpha(\mathbf{x} + e_\alpha \delta t, t + \delta t)$ [Eq. (5)] and $g_\alpha(\mathbf{x} + e_\alpha \delta t, t + \delta t)$ [Eq. (21)].
- **Step 6:** Update the distribution functions (boundary conditions): $h_\alpha(\mathbf{x} + e_\alpha \delta t, t + \delta t)$ [Eq. (40)] and $g_\alpha(\mathbf{x} + e_\alpha \delta t, t + \delta t)$ [Eq. (39)].
- **Step 7:** Update the phase-field variable $\phi(\mathbf{x}, t + \delta t)$ [Eq. (15)], the density $\rho(\mathbf{x}, t + \delta t)$ [Eq. (18)], the relaxation time $\tau(\mathbf{x}, t + \delta t)$ [Eq. (34)], and the viscosity $\mu(\mathbf{x}, t + \delta t)$ [Eq. (19)].
- **Step 8:** Update the normalized pressure $p^*(\mathbf{x}, t + \delta t)$ [Eq. (37)].
- **Step 9:** Update the velocity $\mathbf{u}(\mathbf{x}, t + \delta t)$ [Eq. (38)].
- **Step 10:** Return to Step 3 for the advanced time step.

III. SENSITIVITY ANALYSIS OF THE SOLITARY WAVE SIMULATION

In this section, the selection of the proper grid size, time step and interface thickness for the presented numerical model is conducted.

A. Computational setup

For a solitary wave propagating along the x direction, the water surface of the solitary wave can be expressed as[50]

$$\eta(x, t) = H \mathrm{sech}^2(\theta), \tag{41}$$

where $\theta = (x - X_0 - ct)/\Delta$, X_0 is the initial wave crest position, $c = \sqrt{g d_0 (1 + H_0/d_0)}$ is the wave celerity, $\Delta = d_0 \sqrt{4 d_0 / 3 H_0}$ is the width coefficient of the Korteweg–de Vries (KdV) solution, d_0 is the initial still water depth, H_0 is the initial wave height, and $g = 9.81$ m/s^2 is the gravitational acceleration.

For the initial horizontal and vertical velocities of a point (x, y) in water, there is a method that is more in line with physical reality, that is, replacing the velocity calculation formula in the solitary wave theory with the formula of the cnoidal wave theory (when $m = 1.0$).[56] The velocity expression of the solitary wave can be described by the following equations:

$$\begin{cases} \dfrac{u(x,y,t)}{c} = \dfrac{\eta(x,t)}{d_0}\left[1 - \dfrac{\eta(x,t)}{4d_0} + \left(\dfrac{2d_0^2 - 3y^2}{3\Delta^2}\right) \times \left(2\tanh^2(\theta) - \mathrm{sech}^2(\theta)\right)\right], \\ \dfrac{v(x,y,t)}{c} = \dfrac{2\eta(x,t)y}{d_0\Delta}\left[1 - \dfrac{\eta(x,t)}{2d_0} + \dfrac{2}{3}\left(\dfrac{2d_0^2 - y^2}{\Delta^2}\right) \times \left(\tanh^2(\theta) - 2\,\mathrm{sech}^2(\theta)\right)\right]\tanh(\theta). \end{cases} \tag{42}$$

Computational areas are partitioned into grid spacings dx and time intervals dt. Since LBM is adopted in this study, the length and time conversion coefficient between the lattice constant δx and time step δt of lattice unit (lu) and the macroscopic physical unit is C_l and C_t. The conversion formula is as follows:

$$dx = \delta x \cdot C_l, \tag{43}$$

$$dt = \delta t \cdot C_t. \tag{44}$$

The macroscopic kinematic viscosity and gravitational acceleration are transformed into lattice units (lu) in the following way:

$$v_{LB} = v \frac{dt}{dx^2}\,(\mathrm{lu}), \tag{45}$$

$$g_{LB} = g \frac{dt^2}{dx}\,(\mathrm{lu}), \tag{46}$$

where v and g are the kinematic viscosity and gravitational acceleration, respectively.

For the phase-field model, the mobility $M = 0.08$ in lattice unit[48] is used for all problems. As a note, the above computational setups are used throughout the Subsections III B–V C.

The length (L_x) and height (L_y) of the wave tank for the simulation of a solitary wave on a horizontal bottom are fixed to 16.0 and 0.5 m, respectively. A sketch of the computational domain in this section is given in Fig. 3. The proper grid size, time step, and interface thickness of the numerical model are evaluated through comparisons of the simulation results and the Boussinesq solitary wave theory.[50] We conduct the sensitivity analysis using $H_0/d_0 = 0.3$ ($d_0 = 0.228$ m) as an example. Cyclic boundary conditions are applied in the inlet and outlet conditions, and free-slip boundary conditions are applied in the top and bottom conditions. The simulation results for five different temporal steps, five different spatial steps and four different interface thicknesses are compared in Subsections III B–III D.

B. Spatial step

The details of the numerical tests and the results of the spatial step evaluation are listed in Table II. Different grid sizes of $dx = 1/100$, 1/200, 1/400, 1/500, and 1/800 m are tested in this simulation. A suggested Mach number of 0.0068 is used.[48] To ensure the stability of the simulations, the time step dt varies with the grid size. The wave height of lattice units H_{LB} is defined as $H_{LB} = H_0/\delta x$.

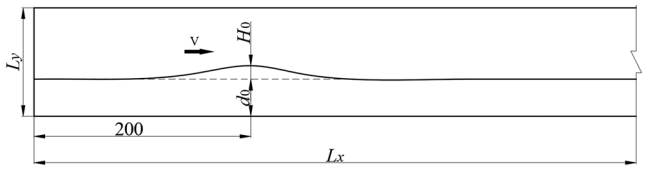

FIG. 3. Sketch of the computational domain (cm).

TABLE I. The basic parameters and simulation results of five different spatial steps.

Group	Number	dx (m)	H_{LB}	dt (s)	Ma_{LB}	$\Delta_{cr,H}$ (%)	$\Delta_{cr,ph}$ (%)
1	1	1/100	7	1/25 000	0.0068	−2.47	1.27
	2	1/200	14	1/50 000	0.0068	0.18	1.13
	3	1/400	27	1/100 000	0.0068	1.10	1.10
	4	1/500	34	1/125 000	0.0068	1.29	1.10
	5	1/800	55	1/200 000	0.0068	1.67	1.18

The wave profiles at the initial time, compared with the wave profiles at the end time, are used to calculate the dissipative error of the wave height,[41]

$$\Delta_{cr,H} = (\eta_{\max,t} - \eta_{\max,t_0})/H_0, \tag{47}$$

where $\eta_{\max,t}$ is the wave crest elevation at $t\sqrt{g/d_0} = 17.55$ and $\eta_{\max,t_0}$ is the initial wave crest elevation.

The discrepancy in the wave phase between the simulated and theoretical results is evaluated by[41]

$$\Delta_{cr,ph} = |x_{cr,s} - x_{cr,t}|/\lambda, \tag{48}$$

where $x_{cr,s}$ is the simulated wave crest position at the end time, $x_{cr,t}$ is the theoretical wave crest position at the end time, and λ is the representative wavelength of the solitary wave.

The dissipative error is shown in Table I. The discrepancy in the wave crests decreases from 2.47% to 0.18% as the grid size dx decreases from 1/100 to 1/200 m. The dissipative error decreases as the grid size decreases. When the grid size decreases to $dx = 1/400$ m, the dissipative error increases to 1.10%. That because the numerical dissipation shows an increasing trend because of too many horizontal grids that can capture the dispersion and nonlinearity.[41] Figure 4 indicates that grid sizes of $dx = 1/200$ ($H_{LB} = 14$) and $dx = 1/400$ ($H_{LB} = 27$) perform better.

C. Temporal step

In the LBM, a proper time step is closely related to the Mach number $\mathrm{Ma}_{LB} = |u|/c_s$. To satisfy the incompressible flow condition, Ma_{LB} should be kept low[48]

$$\mathrm{Ma}_{LB} \ll 1, \quad \text{i.e.,} \quad \frac{|u|\delta t}{\delta x} \ll \frac{1}{\sqrt{3}}.$$

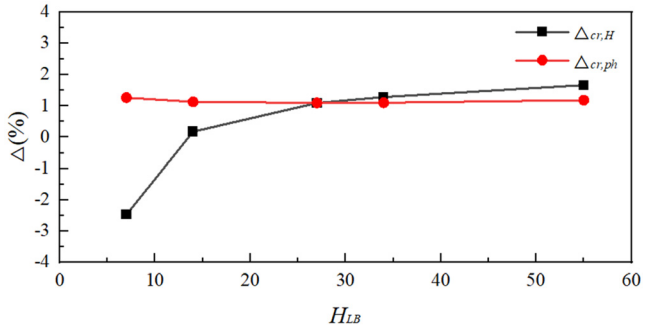

FIG. 4. Dissipative error in the simulations of different spatial steps.

TABLE II. Basic parameters and simulation results for five different temporal steps.

Group	Number	dx (m)	H_{LB}	dt (s)	Ma_{LB}	$\Delta_{cr,H}$ (%)	$\Delta_{cr,ph}$ (%)
2	1	1/200	14	1/20 000	0.0170	0.66	2.92
	2	1/200	14	1/30 000	0.0110	0.48	1.17
	3	1/200	14	1/40 000	0.0085	0.26	1.10
	4	1/200	14	1/50 000	0.0068	0.18	1.13
	5	1/200	14	1/60 000	0.0055	0.18	2.88

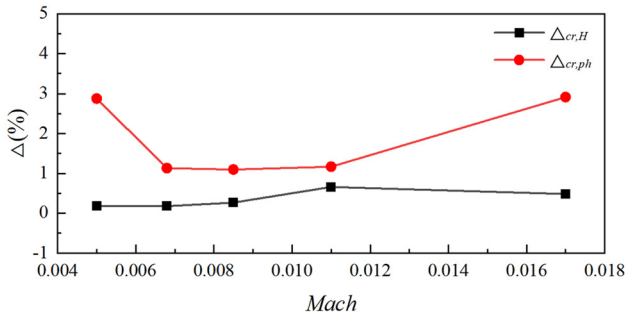

FIG. 5. Dissipative error in the simulations of different temporal steps.

$\mathrm{Ma}_{LB} = 0.0170$, 0.0110, 0.0085, 0.0068, and 0.0055 are tested in the simulations and are listed in Table II. As described earlier, $H_{LB} = 14$ was sufficient, and all the test simulations here maintained $H_{LB} = 14$ or $dx = 1/200$.

From Fig. 5, the wave height dissipative error decreases as the temporal step decreases; however, when the Mach number decreases to $\mathrm{Ma}_{LB} = 0.0055$, the accuracy increases to 2.88%. Overall, the simulated wave agrees best with wave theory for $\mathrm{Ma}_{LB} = 0.0085$ or 0.0068.

D. Interface thickness

The PFLBM simulates the interface layer diffusively with a typical thickness of around five lattice cells.[54] Typically, the interface thickness should be at least an order of magnitude smaller than the smallest characteristic length scale of the system.[55] Additionally, the PFLBM is sensitive to the choice of the interface thickness, which affects the accuracy and numerical stability.[43] To obtain satisfactory simulation results, it is necessary to determine the appropriate interface thickness.

Different interface thicknesses corresponding to $\xi = 2, 3, 4, 5$ are simulated. As shown in Table III, when $\xi = 2$, the calculation

TABLE III. Basic parameters and simulation results for three different interface thicknesses.

Group	Number	dx (m)	H_{LB}	Ma_{LB}	ξ	$\Delta_{cr,H}$ (%)	$\Delta_{cr,ph}$ (%)
3	1	1/200	14	0.0068	2	⋯	⋯
	2	1/200	14	0.0068	3	0.18	1.13
	3	1/200	14	0.0068	4	−0.75	1.20
	4	1/200	14	0.0068	5	−1.68%	1.27%

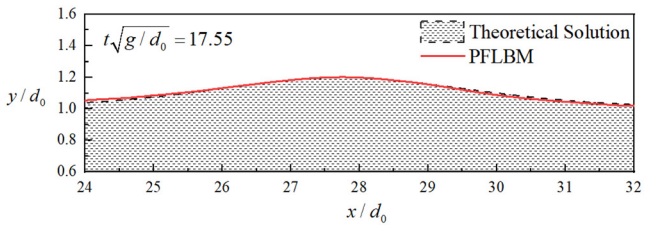

FIG. 6. Spatial wave elevations of the simulated result and theoretical solution for $H_0/d_0 = 0.2$ at $t^* = 17.55$ with $dx = 0.005$ m.

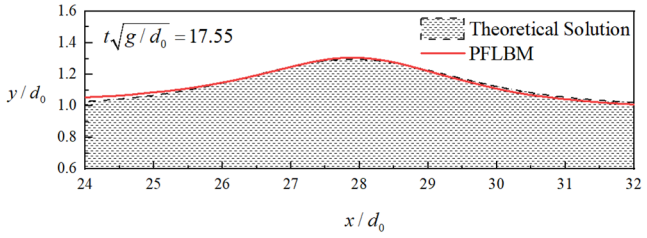

FIG. 7. Spatial wave elevations of the simulated result and theoretical solution for $H_0/d_0 = 0.3$ at $t^* = 17.55$ with $dx = 0.005$ m.

results diverge due to instability, and when $\xi \geq 3$, the accuracy increases as the interface thickness decreases; however, overall, all these errors are within the acceptable range. The results for the interface thickness of $\xi = 3$ most closely agree with the theoretical results. However, to stabilize the sample, it can be appropriately thickened.

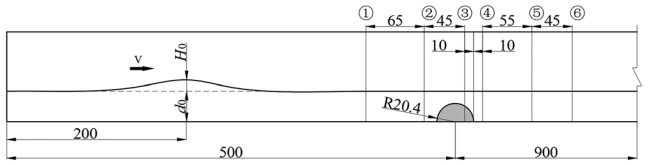

FIG. 8. Sketch of a solitary wave over a semicircular breakwater (cm).

TABLE IV. Parameters for the two experimental cases.

Case	R/d	H_0/d_0	Gauge points
1	0.6	0.311	1, 2, 3
2	0.7	0.514	4, 5, 6

IV. NUMERICAL VALIDATIONS AND COMPARISONS FOR SOLITARY WAVE TRANSFORMATION

This section validates the proposed method through simulations of solitary wave propagation and transformation, specifically for waves on a horizontal bottom and over a submerged breakwater. The simulation results are compared with those from SPH to assess the accuracy of interface capture.

The interface thickness $\xi = 3$ and Mach number $\mathrm{Ma}_{LB} = 0.0068$ in the lattice units and the spatial step $dx = 1/200$ m are used for all the cases in this section.

A. Solitary wave on a horizontal bottom

A rectangular numerical wave tank measuring 0.5 m in height and 16 m in length is employed, with a series of solitary wave

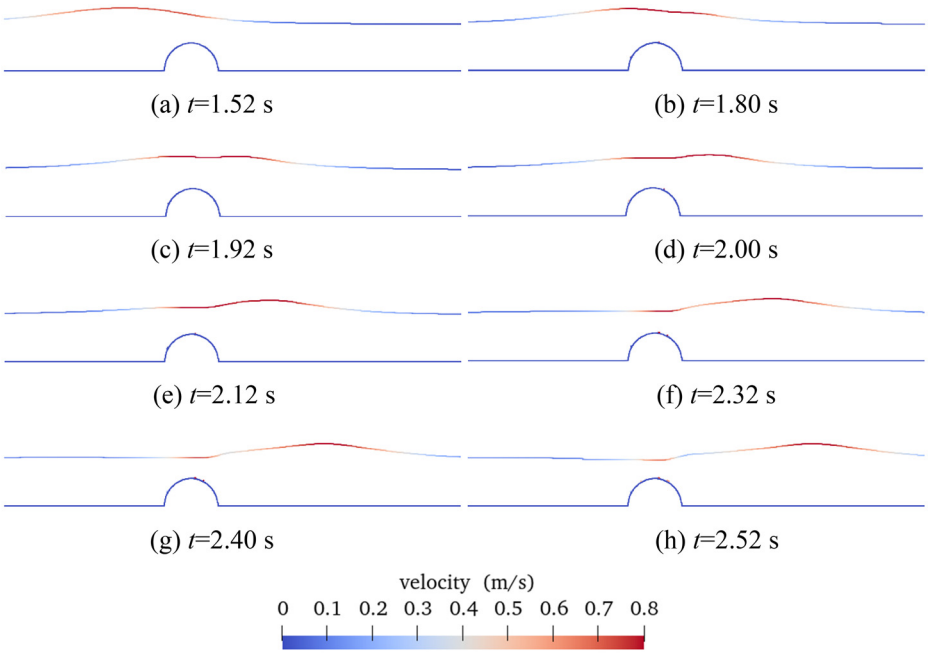

FIG. 9. Simulation results of the velocity of the air–water interface and profile around submerged breakwater in case 1. (a) $t = 1.52$ s, (b) $t = 1.80$ s, (c) $t = 1.92$ s, (d) $t = 2.00$ s, (e) $t = 2.12$ s, (f) $t = 2.32$ s, (g) $t = 2.40$ s, and (h) $t = 2.52$ s.

simulations performed using the PFLBM. The simulated relative wave heights are 0.2 and 0.3, and the initial water depth is 0.228 m.

Figures 6 and 7 compare the wave elevations of the simulated results and theoretical solutions for $H_0/d_0 = 0.2$ and 0.3 at dimensionless time $t^* = t\sqrt{g/d_0} = 17.55$. The wave elevations remain symmetric and agree well with the theoretical solution.

B. Interaction of solitary waves with submerged breakwater

Furthermore, the model is verified by the experiments on solitary wave transformation over submerged semicircular breakwater.[52] In the experiments, a semi-circular submerged underwater with a constant radius of $R = 0.204$ m was affixed to the base of a wave tank. In two different cases, the wave gauges were placed in six locations to obtain the elevation of the solitary wave, as shown in Fig. 8. Table IV lists the experimental parameters and the measurement positions in each case.

The initial crest position was $X_0 = 2$ m. The center of the semicircular breakwater was located at $x = 5$ m. Free-slip boundary conditions were applied at the top, bottom, inlet and outlet boundaries of the numerical wave tank and the structure surface.

1. Solitary wave propagation without breaking over semicircular breakwater

The first simulation (see Table IV-Case 1) illustrates a wave which did not break at any time, and Fig. 9 illustrates that crest–crest exchange occurred across the obstacle.[52]

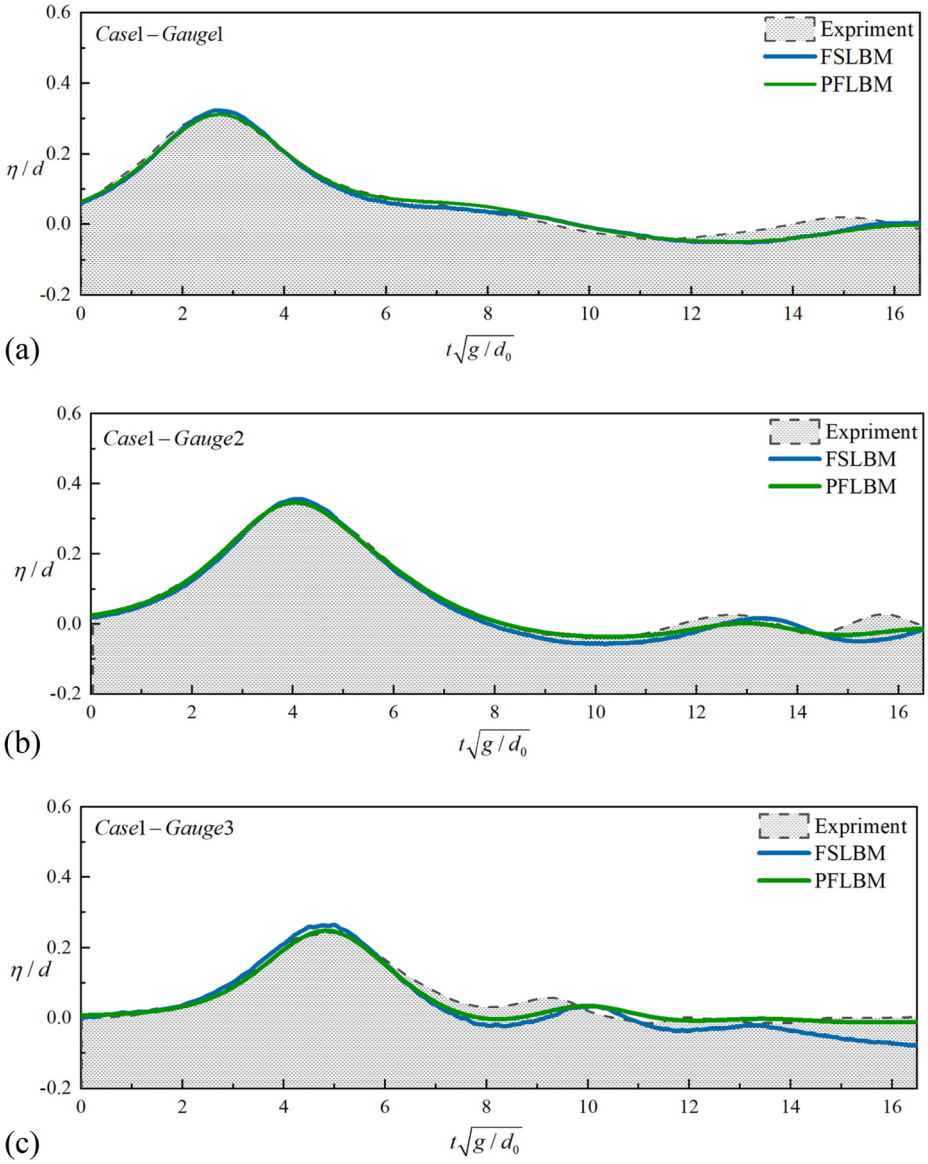

FIG. 10. Comparison of two different numerical results (FSLBM and PFLBM) with the experimental results at three wave gauges in Case1: (a) Gauge 1, (b) Gauge 2, and (c) Gauge 3.

TABLE V. RMSE between the two different numerical results (FSLBM and PFLBM) and the experimental results in case 1.

Case	Gauge points	FSLBM (%)	PFLBM (%)
1	1	1.86	1.72
	2	1.86	1.94
	3	3.51	1.63

The comparison of the wave profiles measured and simulated by the PFLBM and single-phase free surface lattice Boltzmann method (FSLBM)[41] is shown in Fig. 10, which indicates that the numerical simulation results are in good agreement with the experimental results. The root mean square errors (RMSEs) between the two different numerical results (FSLBM and PFLBM) and the experimental results are shown in Table V, and the RMSE can be calculated by

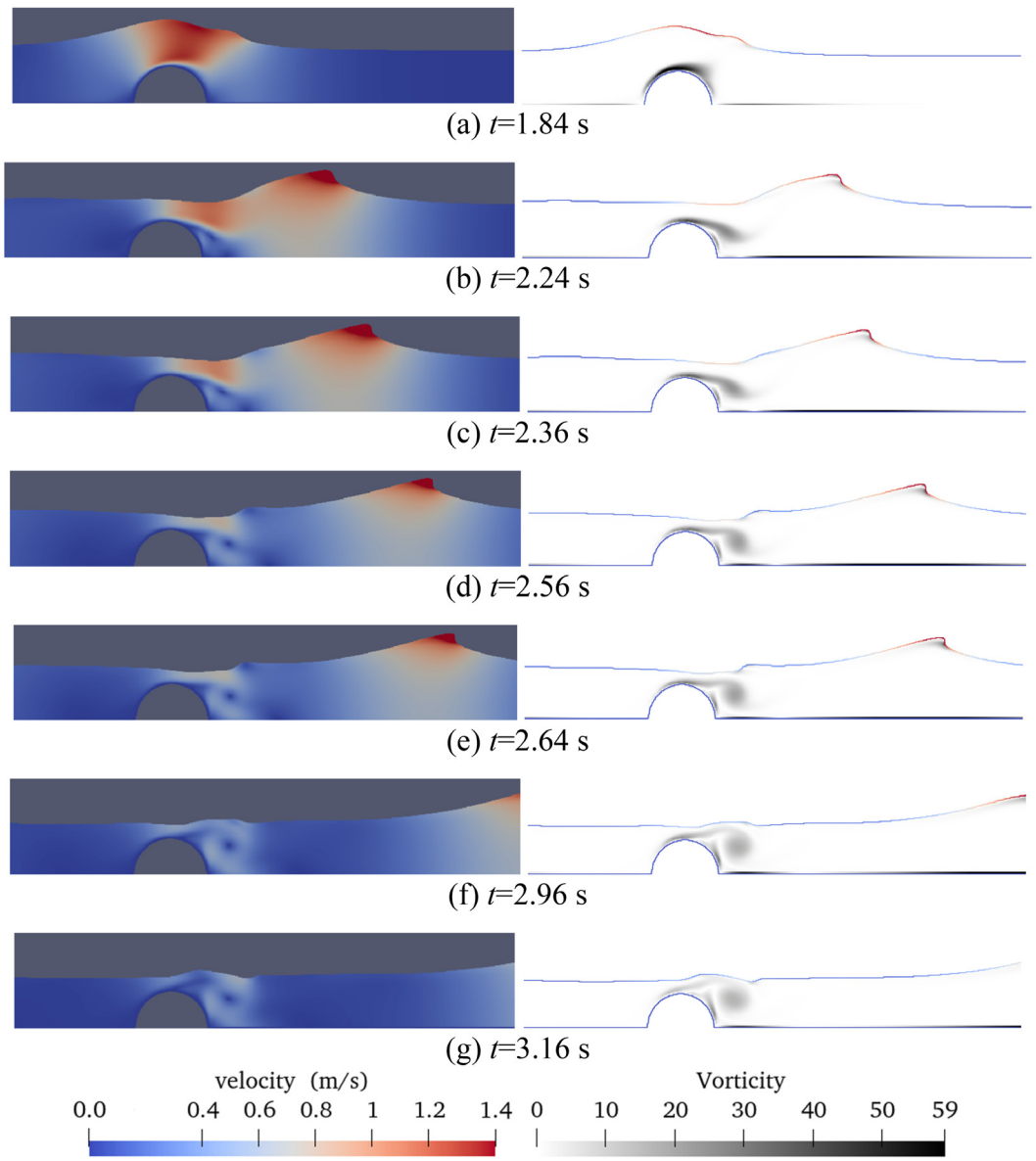

FIG. 11. Simulation results of the velocity and vorticity field and profile around submerged breakwater for case 2. (a) $t = 1.84$ s, (b) $t = 2.24$ s, (c) $t = 2.36$ s, (d) $t = 2.56$ s, (e) $t = 2.64$ s, (f) $t = 2.96$ s, and (g) $t = 3.16$ s.

$$RMSE = \sqrt{\frac{\sum_i^n (\eta_{si} - \eta_{ei})^2}{n}}, \quad (49)$$

where η_{si} is the ith value of the simulated wave profile points, η_{ei} is the ith value of the measured wave profile points, and n is the number of points selected ($n = 100$).

According to Table V, the results of the PFLBM agree with the experimental results better than those of the FSLBM, especially at Gauge 3, which is behind the submerged level.

2. Solitary wave propagation with breaking over semicircular breakwater

With the higher H_0/d_0 in this simulation (see Table IV-Case 2), the solitary wave exhibited a forward breaker and backward breaker.[52] When the solitary wave interacts the semi-circular underwater, an eddy forms on its surface, as shown in Fig. 11 ($t = 1.84$–2.24 s). As the wave propagates forward, the eddy on the underwater surface is lifted and develops on the downstream side of the underwater ($t = 2.24$–3.16 s). When the backward breaker propagates forward ($t = 3.16$ s), a small level drop appears. The results are in full agreement with the numerical simulations of Han *et al.*[51]

The comparison of the wave profiles measured and simulated by the PFLBM and FSLBM[41] at the same resolution is shown in Fig. 12. The RMSEs between the two different numerical results (FSLBM and PFLBM) and the experimental results are listed in Table VI. From Figs. 11(a) and 11(b), a forward breaker occurred, and the profile shows strong increase in surface steepness corresponding to the rapid rise of the wave surface at nondimensional time 6.5 and 8.0 in Fig. 12, at Gauges 5 and 6, respectively. It can be seen from the data in Table VI that the RMSEs of PFLBM is relatively small, especially at Gauge 6.

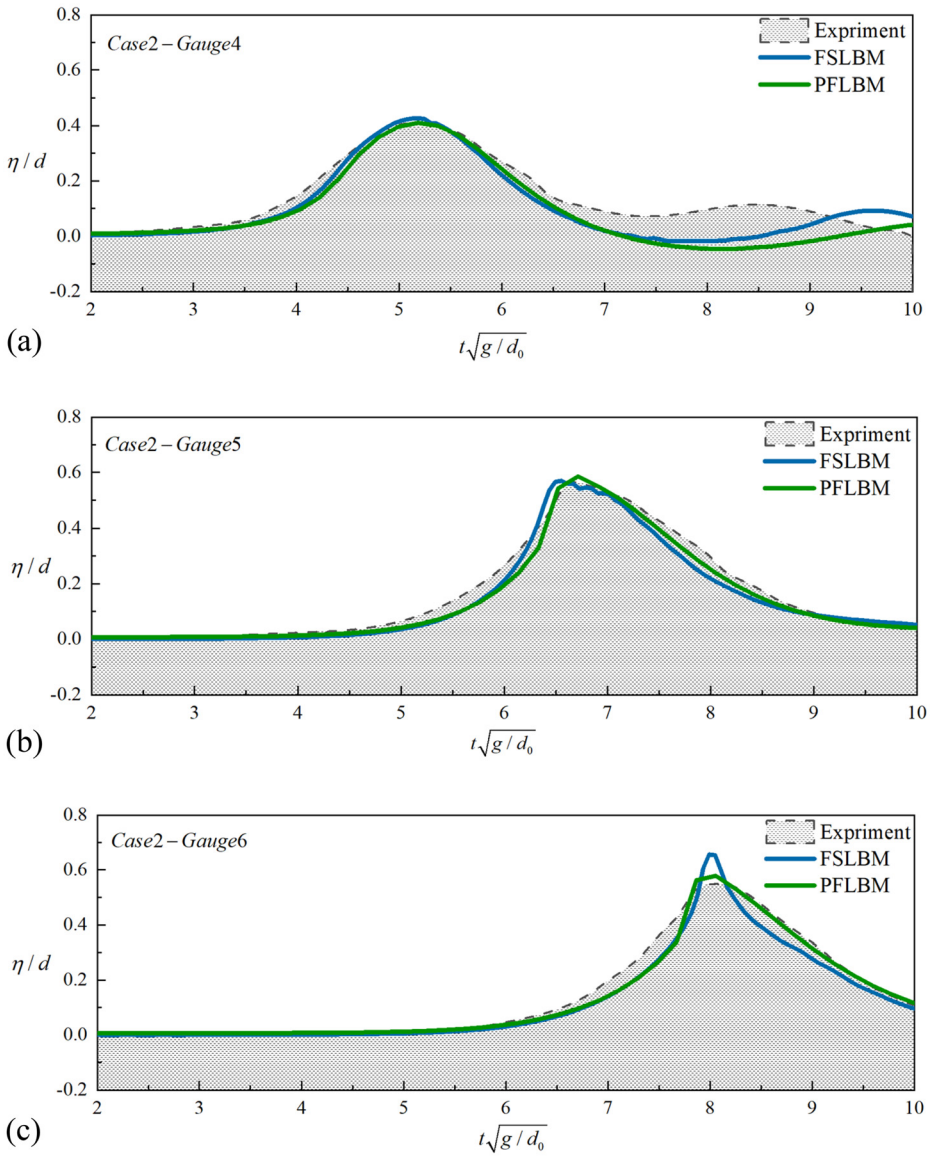

FIG. 12. Comparison of two different numerical results (FSLBM and PFLBM) with the experimental results at three wave gauges in case 2: (a) Gauge 4, (b) Gauge 5, and (c) Gauge 6.

TABLE VI. RMSE between the two different numerical results (FSLBM and PFLBM) and the experimental results in case 2.

Case	*Gauge points*	FSLBM (%)	PFLBM (%)
2	4	4.30	4.88
	5	2.61	2.38
	6	3.05	2.45

In conclusion, it is found that the results simulated by PFLBM are more consistent with the experimental results, which indicates that PFLBM is reliable in simulating the interaction between solitary waves and the submerged breakwater, especially in terms of wave breaking. The main difference of the experimental and PFLBM numerical results is the part after the wave crest crosses the submerged breakwater in case 2-Gauge 4. This phenomenon arises from differences in the wave generation methods used: laboratory wave generation, the single-phase flow numerical wave tank method, and the initial wave profile in our two-phase flow model. The presence of a wave generation boundary, where the inflow $Q_0 > 0$ at the entrance (left boundary of the numerical wave tank),[57] introduces non-hydrostatic effects that result in variations in the final results.

C. Two different computational models for simulations of wave transformation

In this section, the ability of PFLBM and smoothed particle hydrodynamics (SPH)[51] to simulate the solitary wave transformation over submerged breakwater is compared. The parameters of the cases are the same as those in Sec. IV B. The spatial steps (for SPH is the particle sizes) are $dx = 0.005$ m ($dp = 0.005$ m) and $dx = 0.001$ m ($dp = 0.001$ m) to compare the interface capture accuracy of the two models with the same accuracy and the improvement of the accuracy of the finer grid.

The comparisons of the wave profiles measured and simulated by the SPH and PFLBM is shown in Figs. 13 and 14. The RMSEs between the two different numerical results (SPH and PFLBM) and the experimental results are shown in Table VII. From them, we found that these two numerical simulation results are both in good agreement with the experimental results for both breaking and nonbreaking cases and their simulation accuracy is comparable. As the grid is refined (as particle sizes decreased), the simulation accuracy of both methods improves, especially the root mean square error of PFLBM decreasing by as much as 4.5%.

V. SIMULATION RESULTS OF SOLITARY WAVE BREAKING

This section uses PFLBM to simulate three typical solitary wave breaking behaviors on a beach slope. It briefly analyses the differences

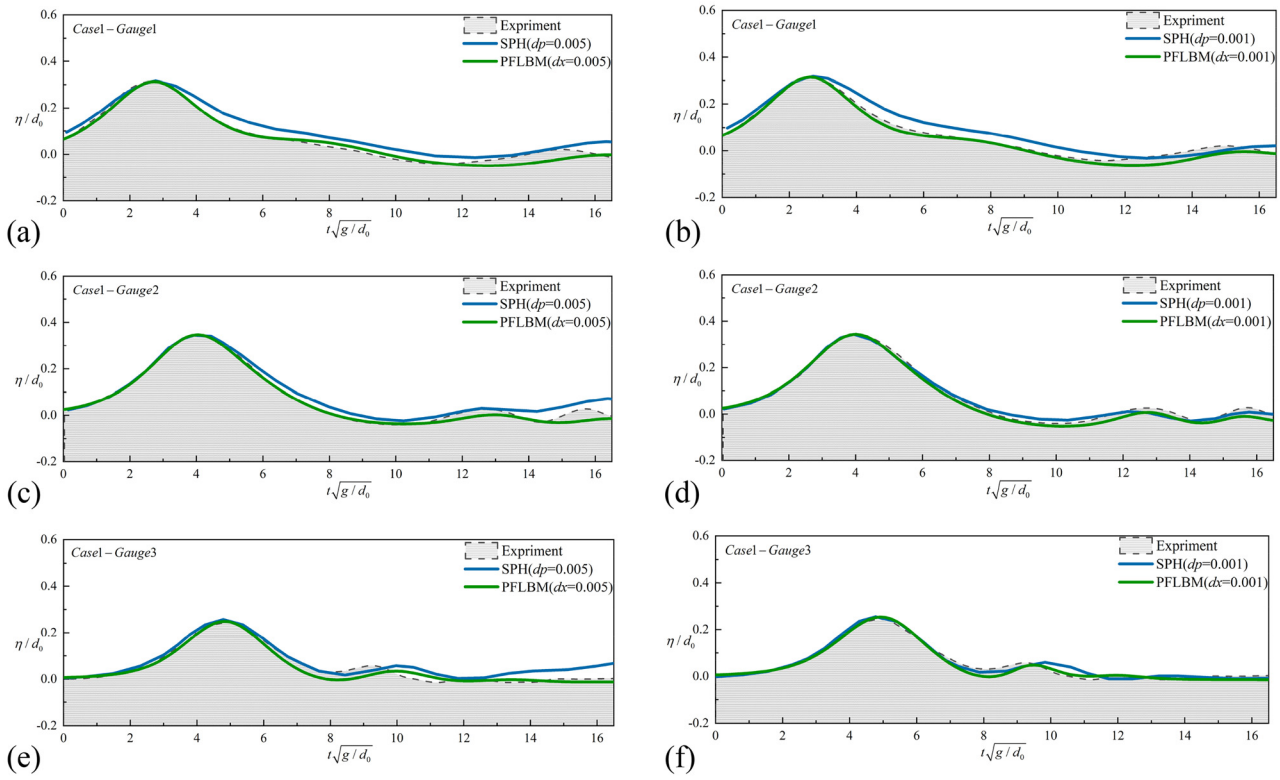

FIG. 13. Comparison of two different numerical results (SPH and PFLBM) with the experimental results at three wave gauges in case 1: (a) Case1-Gauge 1 and spatial step $dx = 0.005$, (b) case 1-Gauge 1 and spatial step $dx = 0.001$, (c) case 1-Gauge 2 and spatial step $dx = 0.005$, (d) case 1-Gauge 2 and spatial step $dx = 0.001$, (e) case 1-Gauge 3 and spatial step $dx = 0.005$, and (f) case 1-Gauge 3 and spatial step $dx = 0.001$. [Data of SPH from Han *et al.* (2020).[51]]

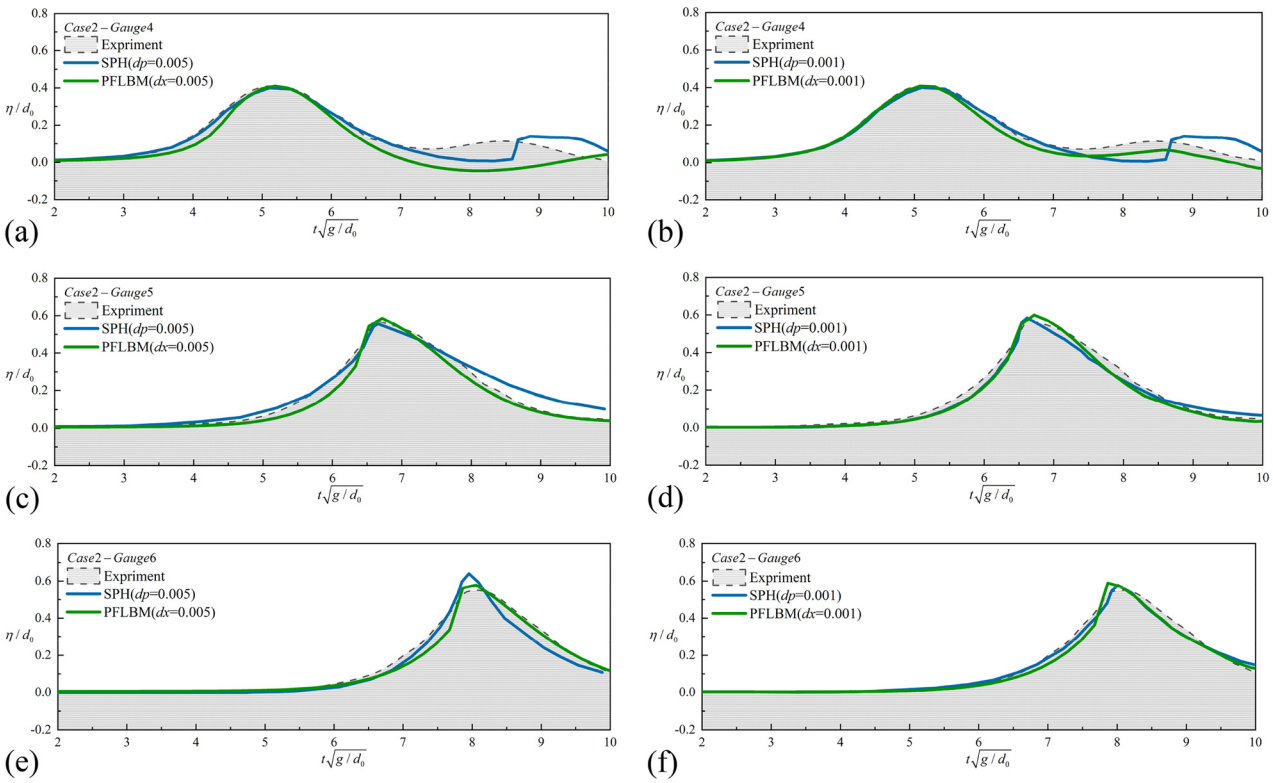

FIG. 14. Comparison of two different numerical results (SPH and PFLBM) with the experimental results at three wave gauges in case 2: (a) Case 2-Gauge 4 and spatial step $dx = 0.005$, (b) case 2-Gauge 4 and spatial step $dx = 0.001$, (c) case 2-Gauge 5 and spatial step $dx = 0.005$, (d) case 2-Gauge 5 and spatial step $dx = 0.001$, (e) case 2-Gauge 6 and spatial step $dx = 0.005$, and (f) case 2-Gauge 6 and spatial step $dx = 0.001$. [Data of SPH from Han *et al.* (2020).[51]]

in breaking positions and air entrainment among various breaker types, with a particular focus on the instantaneous flow characteristics of plunging breakers. By comparing the evolution of kinetic energy, potential energy, and total energy during wave breaking, this section explores the differences between single-phase and two-phase flow simulations and examines the impact of kinetic energy transfer between water and air on energy dissipation during wave breaking.

As shown in Fig. 15, the initial crest position of the solitary wave is set at X_0. In addition, the wave moves horizontally. The problem's other parameters are defined as follows: d_0 is the initial still water depth, H_0 is the initial wave height, s is the slope steepness, and $B = 5d_0$ is the horizontal length from the crest to the foot of the slope. The interface thickness $\xi = 3$ in the lattice units, Mach number $\mathrm{Ma}_{LB} = 0.0068$ and spatial step $dx = 1/200$ m are used for all the cases in this section. Free-slip boundary conditions are again applied at the top, bottom, inlet, and outlet.

TABLE VII. RMSE between the two different numerical results (SPH and PFLBM) and the experimental results in case 1 and case 2.

Case	Gauge points	SPH (%)		PFLBM (%)	
		$dp = 0.005$	$dp = 0.001$	$dx = 0.005$	$dx = 0.001$
1	1	3.06	2.02	1.72	1.21
	2	3.06	0.98	1.94	0.97
	3	2.63	1.46	1.63	1.33
2	4	2.85	2.50	4.88	0.36
	5	3.14	2.19	2.38	2.05
	6	4.49	1.97	2.45	2.23

A. Typical wave breakers

A dimensionless parameter S_0 was introduced by Grilli *et al.*[22] for predicting the types of solitary wave breaking

$$S_0 = 1.521 \frac{s}{\sqrt{\frac{H_0}{d_0}}}. \tag{50}$$

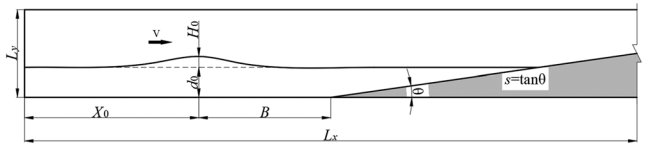

FIG. 15. Sketch of a solitary wave on a beach slope.

TABLE VIII. Parameters for the three types of breakers.

Case	Breaker types	H_0/d_0	s	S_0
1	Plunging	0.60	1/15	0.13
2	Surging	0.35	1/8	0.32
3	Spilling	0.40	1/120	0.02

Here, (i) $S_0 < 0.025$ indicates a spilling breaker, (ii) $0.025 < S_0 < 0.30$ indicates a plunging breaker, (iii) $0.30 < S_0 < 0.37$ indicates a surging breaker, and (iv) $S_0 > 0.37$ indicates nonbreaking.

In this section, the three types of breakers are simulated, and the solitary wave parameters, as listed in Table VIII, are chosen according to the above criteria. The numerical wave tank was reduced to 7, 10, and 26 m, respectively, and the initial crests were located at $x_0 = 2$, 3, and 3 m.

1. Plunging breaker

Figure 16 shows the evolution of the free surface with $H_0/d_0 = 0.60$ and $s = 1/15$, where $S_0 = 0.13$ indicates a plunging breaker. With wave propagation, the front face of solitary wave becomes vertical and then curls, leading to the formation of a water jet that plunges onto the wave front face. Then a cavity is created under the curly wave crest. The water jet hits the wave surface, causing it to splash into the air.

Figure 17 shows the time evolution of the grid quantity of the mixture of air and water, the dimensionless volume of entrained water and volume of entrained air. The mixture is characterized by the

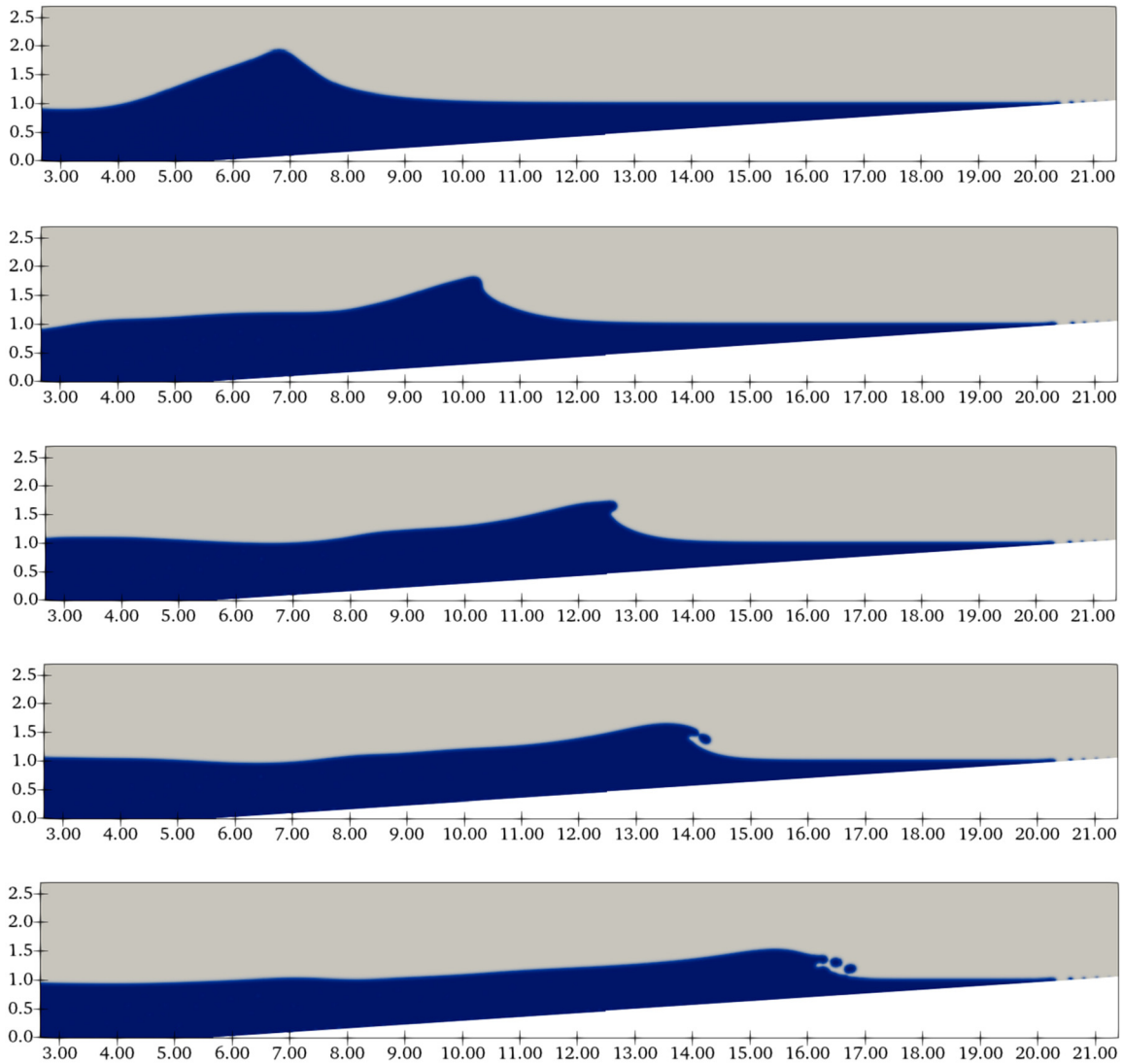

FIG. 16. Evolution of free surface profiles for a plunging breaker with $H_0/d_0 = 0.60$ and $s = 1/15$ (the x axis and y axis are normalized by d_0).

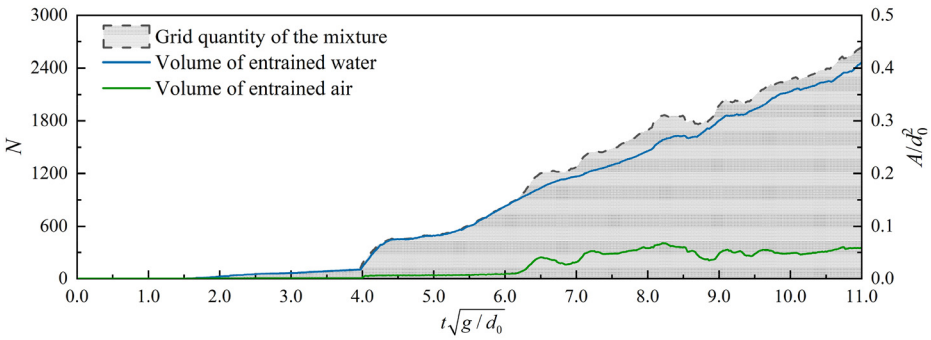

FIG. 17. Time evolution of the grid quantity of the mixture, the dimensionless volume of entrained water and volume of entrained air of the plunging breaker.

region between the upper bound and the lower bound of the interface. As pointed out by Yang *et al.*,[53] some small droplets can be convected far from the surface of wave; therefore, it is feasible to choose the appropriate phase-field value to define the upper bound, and $\phi = 1.0 \times 10^{-6}$ is adopted in this study. The mixture of air and water is between the upper ($\phi = 1.0 \times 10^{-6}$) and lower bounds ($\phi = 1.0 - 1.0 \times 10^{-6}$) of the interfaces. The volume of entrained water $A_{water}(t)$ and volume of entrained air $A_{air}(t)$ is defined by

$$A_{water}(t) = \sum_{i=1}^{N(t)} \phi_i(t) \cdot dx^2, \tag{51}$$

$$A_{air}(t) = \sum_{i=1}^{N(t)} (1 - \phi_i(t)) \cdot dx^2, \tag{52}$$

where $N(t)$ is the grid quantity of the mixture, $\phi_i(t)$ is the phase-field value of the ith grid.

It can be seen in Fig. 17 that the volume of entrained air increases rapidly at the dimensionless time $t_b\sqrt{g/d_0} = 4.0$, indicating the start of wave breaking. At this moment, the breaking position is at $x_b/d_0 = 9.7$, some distance from the initial shoreline. Figure 18 illustrates the velocity vectors of the plunging wave and the air entrainment within the mixture. It is evident that the wave crest plunges forward and impacts the water surface ahead of the crest, leading to the type of plunging breaker. For plunging breakers, air entrainment occurs due to the formation of a water jet at the top of the wave, which projects forward and entrains air as it collides with the water surface in front of the wave.

2. Surging breaker

With $H_0/d_0 = 0.35$ and $s = 1/8$ in this case, as shown in Fig. 19, it is the surging breaker. As the wave propagates from deep water to shallow water, the wave front steepens and the crest gradually becomes asymmetrical. The wave breaks from the bottom of the wave front, as described in Fig. 19.

When the type of breaker changes from the plunging breaker to the surging breaker, the breaking occurs in a narrower region closer to the shoreline, and the breaking depth decreases.[33] Figure 20 shows that the surging wave begins to break at time $t_b\sqrt{g/d_0} = 6.5$, with the breaking position $x_b/d_0 = 0.1$ located near the initial shoreline. Figure 21 indicates that the wave breaks from the bottom of the wave front, significantly influenced by a steeper slope, and the volume of air entrained is limited to a small portion at the base of the wave front.

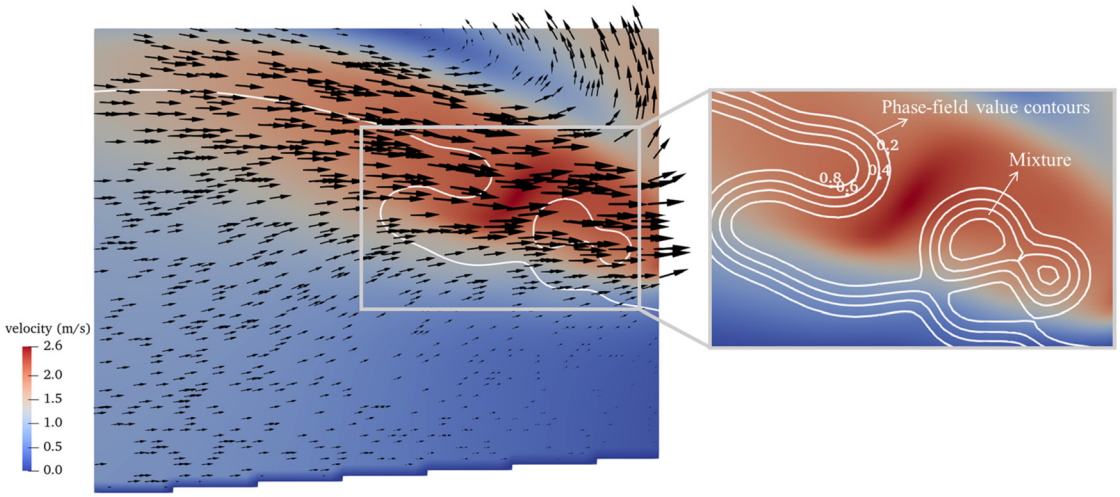

FIG. 18. Velocity vectors and the air entrainment within the mixture of the plunging breaker.

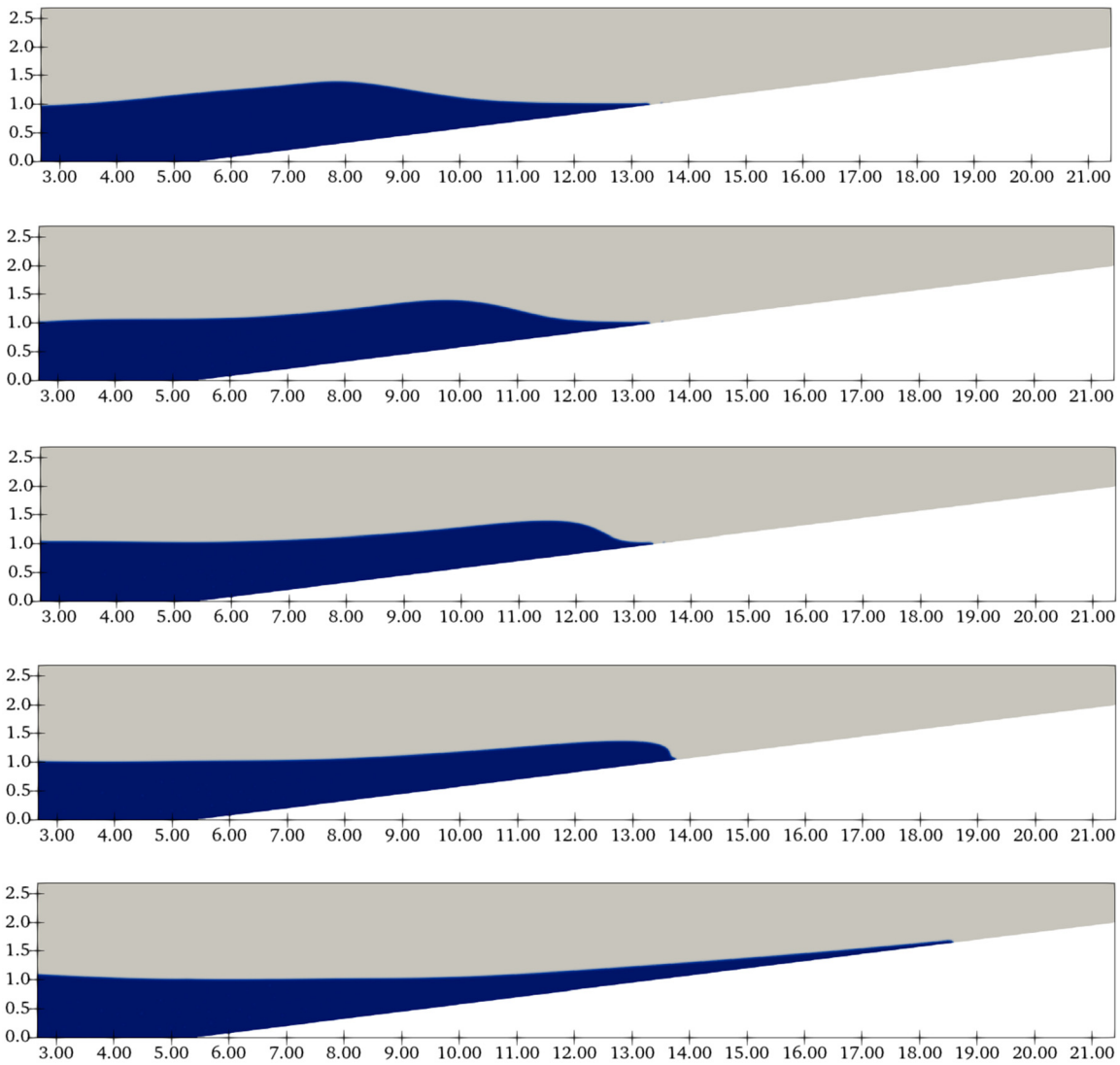

FIG. 19. Evolution of free surface profiles for a surging breaker with $H_0/d_0 = 0.35$ and $s = 1/8$ (the x axis and y axis are normalized by d_0).

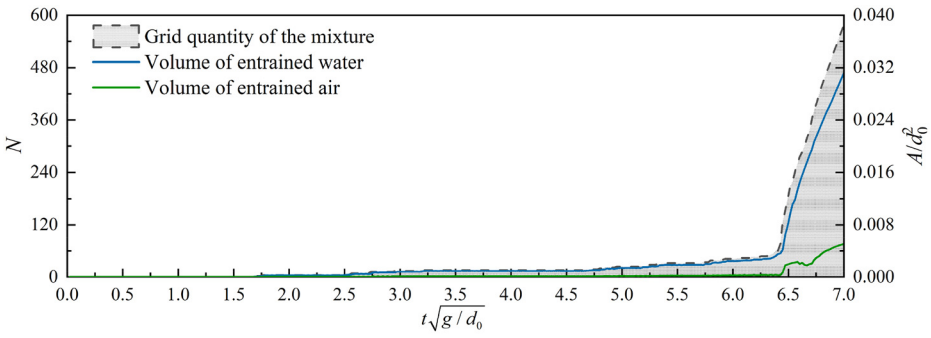

FIG. 20. Time evolution of the grid quantity of the mixture, the dimensionless volume of entrained water and volume of entrained air of the surging breaker.

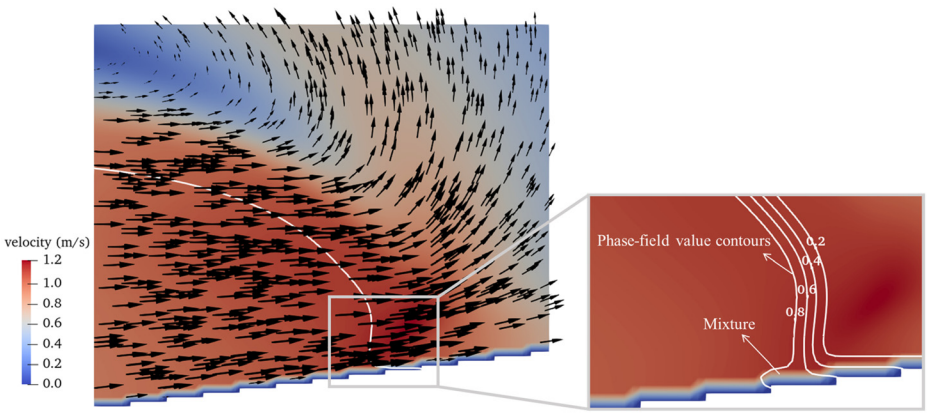

FIG. 21. Velocity vectors and the air entrainment within the mixture of the surging breaker.

3. Spilling breaker

Simulated parameters $H_0/d_0 = 0.4$ and $s = 1/120$ are set in this case, as shown in Fig. 22. This type of breaking wave (spilling breaker) occurs in deep water when the wave steepness is relatively large and the bottom slope is relatively flat. It behaves similarly to a plunging breaker in the early stage, but it does not experience flow separation.

As the breaker type transitions from plunging to spilling, the breaking occurs farther from the shoreline, and the breaking depth increases. Figure 23 shows that the solitary wave begins to break at

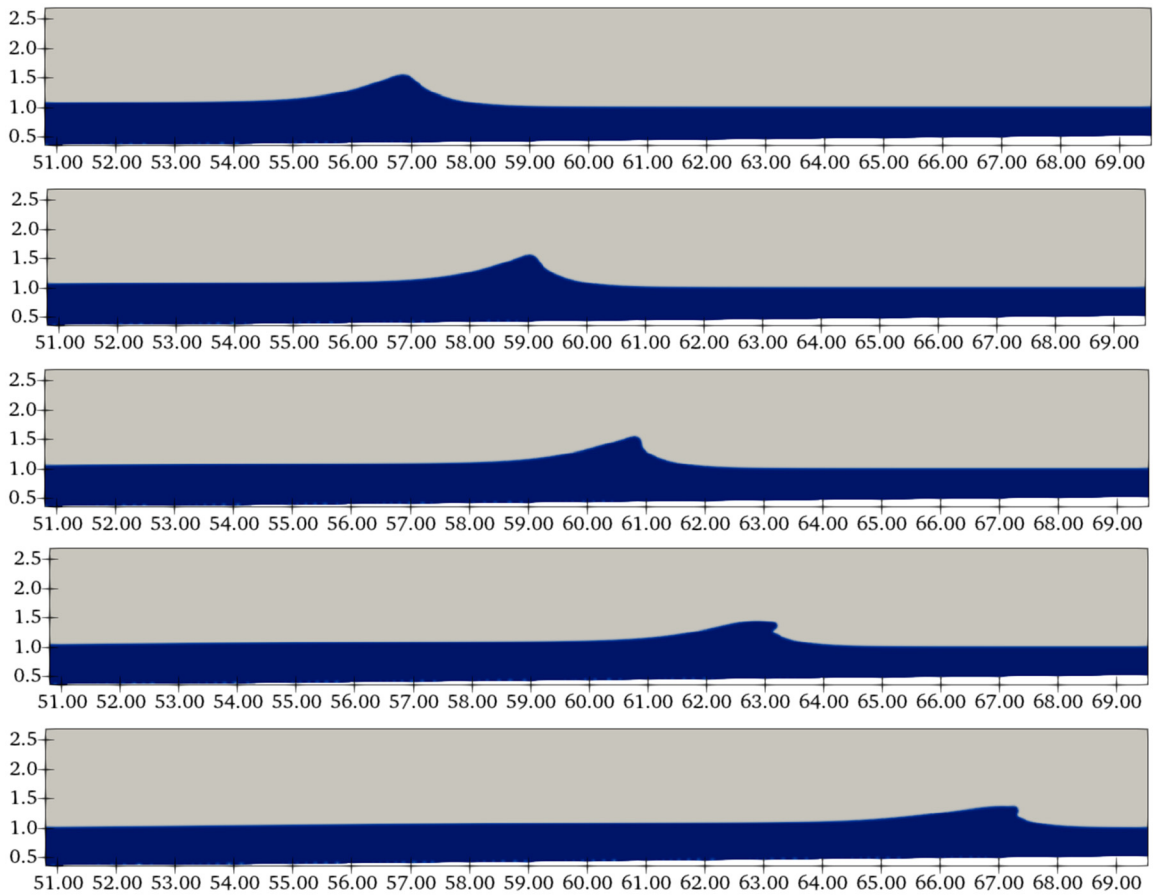

FIG. 22. Evolution of free surface profiles for a spilling breaker with $H_0/d_0 = 0.40$ and $s = 1/120$ (the x axis and y axis are normalized by d_0).

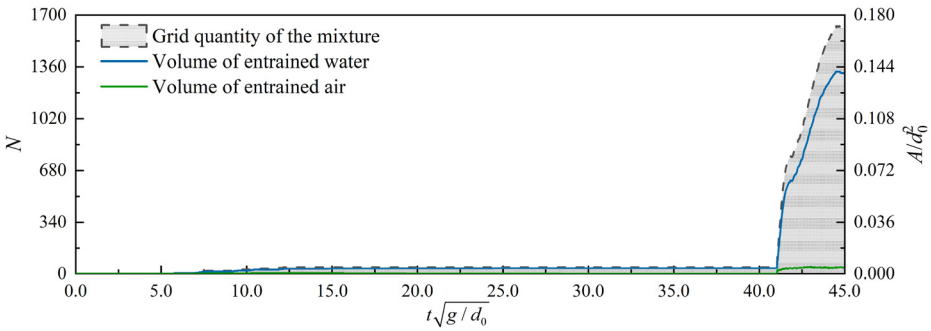

FIG. 23. Time evolution of the grid quantity of the mixture, the dimensionless volume of entrained water and volume of entrained air of the spilling breaker.

time $t_b\sqrt{g/d_0} = 41.0$ with the breaking position at $x_b/d_0 = 62.8$. Figure 24 illustrates that a small patch of turbulence appears at the crest of the wave during breaking, with the leading edge of this turbulence spilling over the front surface of the wave. Air entrainment moves with the waves, behaving like a surface roller before eventually being absorbed into the water. Compared to plunging breakers, spilling breakers typically generate weaker turbulence and entrain less air.

B. Instantaneous flow characteristics of breaking waves

Taking the plunging breaker as an example to discuss the instantaneous flow characteristics during the breaking of solitary wave.

As demonstrated in Fig. 25(a), when the wave is onset to break, the vertical velocity is positive on the rear surface and negative on the front surface.[53] Therefore, an air vortex is generated between the downward and upward airflow. Figure 26 more clearly shows the air vortex that appears near the wave crest, showing that the solitary wave has begun nonlinear propagation. Figures 26(a)–26(d) show that the air vortex continues to move with the propagation of the solitary wave. Despite significant deformation of the wave surface, the air vortex consistently remains near the solitary wave.

The overturning jet shown in Fig. 27 significantly alters the flow structures during the plunging event. When the jet hits the wave front face, a high-speed region is formed in front of the solitary wave [Figs. 27(a-1) and 27(b-1)]. At the same time, the jet causes the surrounding air to hit the wave surface. As a result, the vertical velocity of the air shown in Figs. 27(a-2) and 27(b-2) becomes negative above the wave crest.

Figures 25(a), 25(b), 27(a), and 27(b) show that the maximum value of U increases by 27.8% at $t* = 3.62$ and by 47.1% at $t^* = 6.08$, but then decreases by 36% at $t* = 7.09$ after the wave breaks. This indicates that, after breaking, the water wave ceases to transfer momentum to the air vortex, which aligns with the observations of He *et al.*[19]

Figure 27 uses a bold black line to delineate the upper bounds ($\phi = 1.0 \times 10^{-6}$) of the interfaces of water and air. Air entrainment is primarily concentrated between this upper bound ($\phi = 1.0 \times 10^{-6}$) and the air–water free surface ($\phi = 0.5$). The air on the wave crest hits the wave surface, and the air in front of the wave crest is pushed away, forming a counterclockwise vortex, in accordance with the air vortex marked in Figs. 26(c) and 26(d). This counterclockwise vortex corresponds to the positive vorticity in Figs. 27(a-3) and 27(b-3). A small clockwise-rotating vortex (2) is generated below the large vortex (1), which corresponds to the negative vorticity in Figs. 27(a-3) and 27(b-3). This shows that the mixture of air and water tends to roll into the water, which reveals the flow structures of the plunging breaker caused by air entrainment.

C. Energy dissipation

Since the nonlinear characteristics of the breaking solitary waves are related to the slope and the wave height, the simulated cases are divided into three groups to investigate the kinetic energy evolution of water and air during wave breaking. The parameters for different cases are listed in Table IX.

1. Kinetic energy of water

In this section, we calculate the time evolution of the kinetic energy of the water. The kinetic energy $E_{k,t}$ is defined by

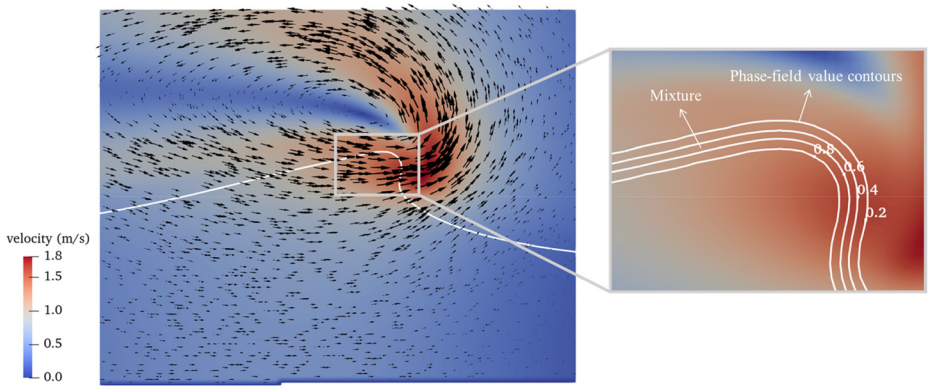

FIG. 24. Velocity vectors and the air entrainment within the mixture of the spilling breaker.

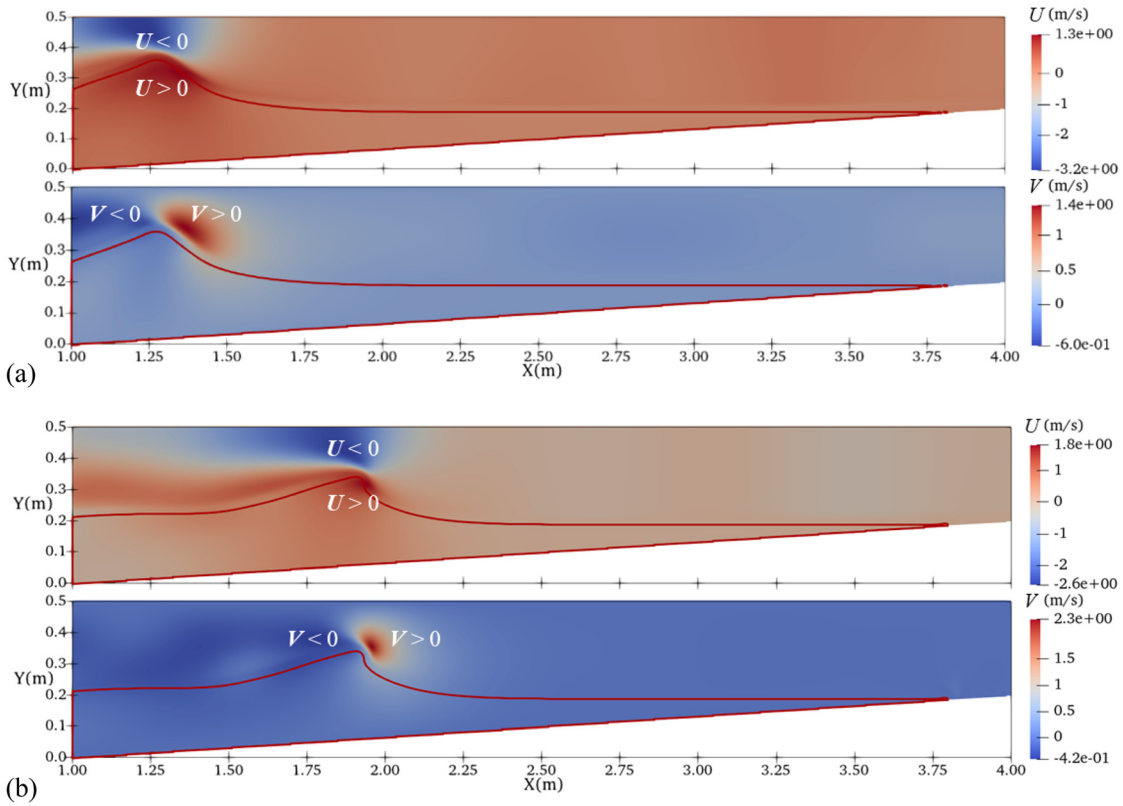

FIG. 25. Instantaneous horizontal velocity (U) and vertical velocity (V) distributions before the wave breaks: (a) $t^* = 1.30$ and (b) $t^* = 3.62$. The red line represents the wave surface.

$$E_{k,t} = \sum_{i=1}^{N} \frac{1}{2} \rho_i dx^2 (u_i^2 + v_i^2), \tag{53}$$

where N is the grids number of the water phase, ρ_i is the ith density of the water, and u_i and v_i are the ith horizontal and vertical velocity of the water.

According to He *et al.*,[19] the time evolution of the wave kinetic energy during wave breaking can be divided into three stages, i.e., the energy propagation stage, the energy dissipation stage and the energy conservation stage. Figure 28 shows that the results of the PFLBM and FSLBM are both consistent with the observations of He *et al.*[19]

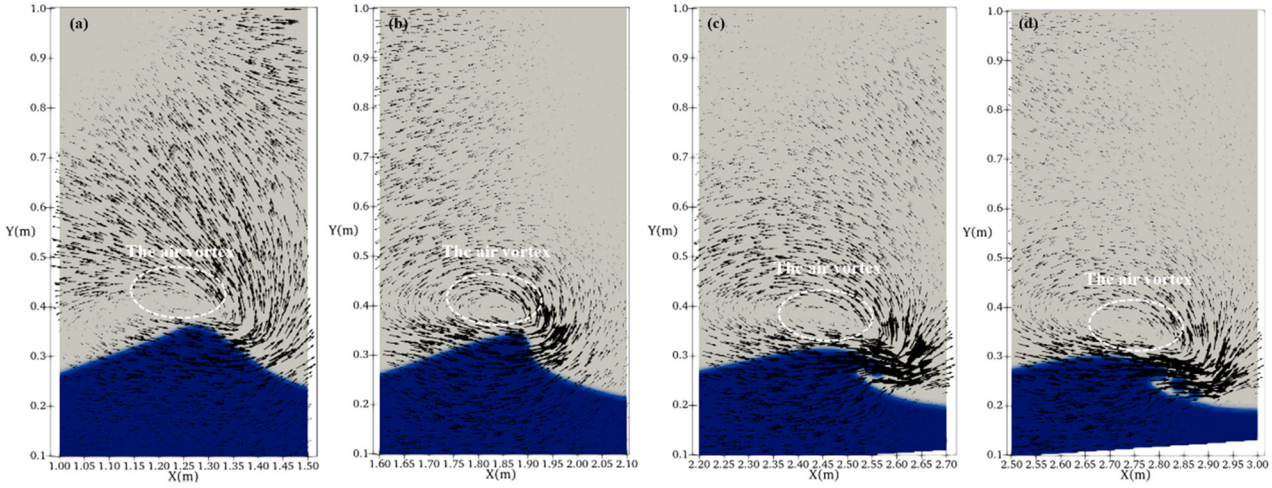

FIG. 26. Instantaneous velocity vector distribution before the wave breaks: (a) $t* = 1.30$; (b) $t* = 3.62$; (c) $t* = 6.08$; and (d) $t* = 7.09$.

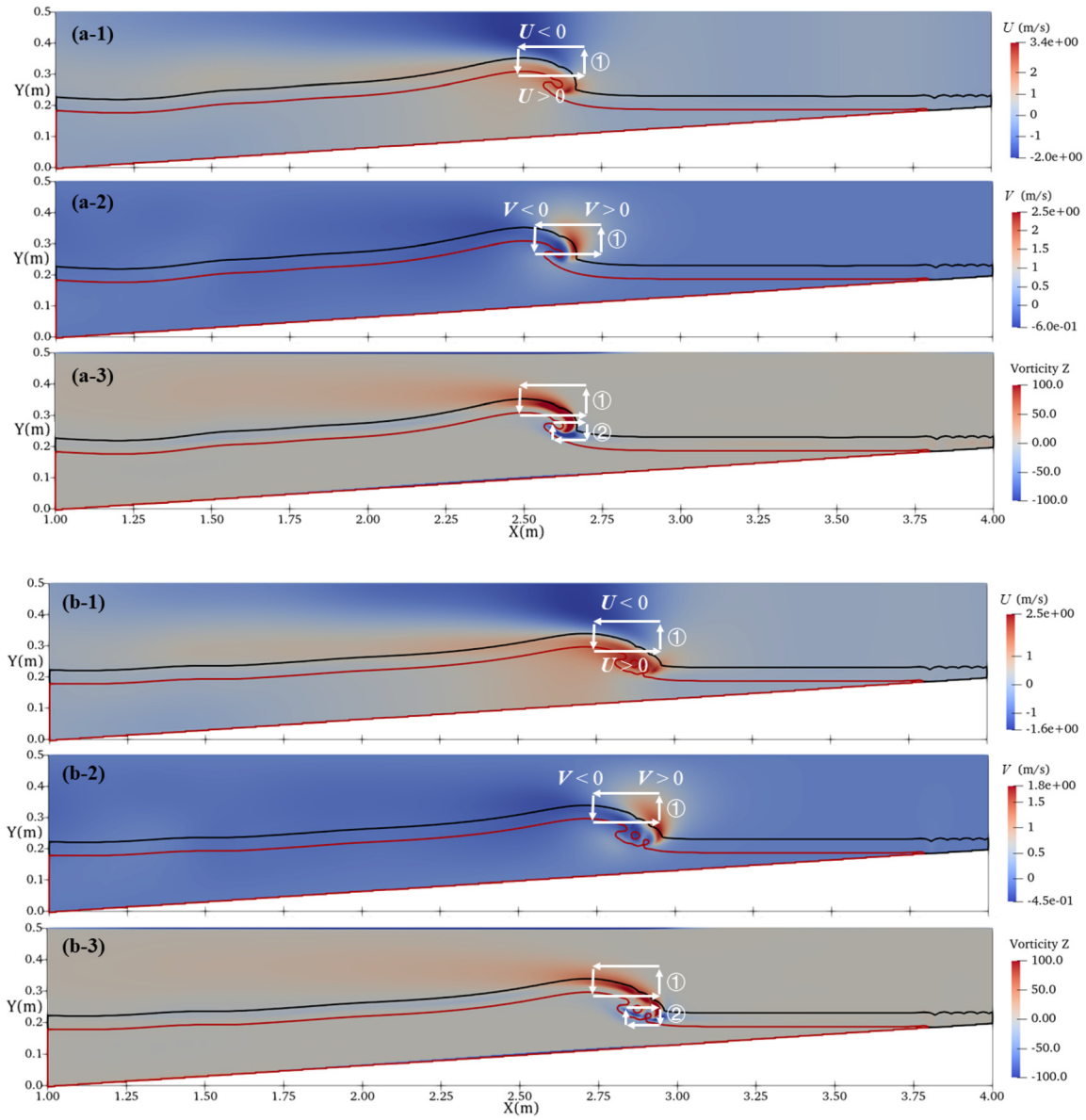

FIG. 27. Instantaneous streamwise velocity (U) and vertical velocity (V) distributions and the vorticity field near the wave surface after the wave breaks: (a) $t* = 6.08$ and (b) $t* = 7.09$. The red line represents the wave surface, and the black line represents the upper bound of the interfaces.

From the results of the PFLBM, when the wave breaking begins, the kinetic energy decreases with time until it reaches its minimum value at the maximum run-up. According to the experiments conducted by Li *et al.*,[9] the duration of the energy dissipation in nondimensional time $t\sqrt{g/d_0}$ is ∼10 with $H/d_0 = 0.3$ on a 1/15 slope. According to Fig. 28(b), the non-dimensionality of the energy dissipation of the PFLBM is ∼10, and that of the FSLBM is ∼5.

In conclusion, compared with the results of the single-phase model (FSLBM), in which the kinetic energy dissipation speed is too high, the water kinetic energy simulated by the two-phase model (PFLBM) in this study is closer to the actual wave breaking. Therefore, the air phase helps improve the accuracy of the breaking wave simulation.

2. Kinetic energy of air

Figure 29 shows the evolution of air kinetic energy over time during the wave breaking in different cases. The evolution of air energy can be divided into three stages as well. In the first stage, the air absorbs energy from the water. Since the wave has not yet broken, the energy transfer is relatively small, making the air energy maintain a relatively small change. During the second phase, wave breaks and

TABLE IX. Parameters for different cases.

Group	Case	H_0/d_0	s	S_0
1	1	0.30	1/10	0.28
	2	0.40	1/10	0.24
	3	0.50	1/10	0.22
	4	0.60	1/10	0.20
2	5	0.30	1/15	0.19
	6	0.40	1/15	0.16
	7	0.50	1/15	0.14
	8	0.60	1/15	0.13
3	9	0.30	1/20	0.14
	10	0.40	1/20	0.12
	11	0.50	1/20	0.11
	12	0.60	1/20	0.10

generates the plunging jet, resulting in the entrainment of air in the water wave. At this stage, the kinetic energy of the air increases significantly during wave breaking and peaks after the breaking. It can be concluded that kinetic energy is continuously transferred from water to air during the wave plunging. According to Fig. 28, the breaking time increases with increasing relative wave height. The time to reach the maximum kinetic energy with a larger relative wave height occurs earlier. In the third stage, the kinetic energy of water is very low, and it stops transporting kinetic energy to the air. Therefore, the air energy continues to dissipate until it disappears.

3. Potential energy, total energy, and energy dissipation

In this section, we calculate the time evolution of the potential energy and total energy of the water. The potential energy $E_{p,t}$ and total energy $E_{m,t}$ is defined by

$$E_{p,t} = \sum_{i=1}^{N} \frac{1}{2} \rho_i dx^2 g y_i, \tag{54}$$

$$E_{m,t} = E_{k,t} + E_{p,t}, \tag{55}$$

where y_i is the height of the ith grid.

According to Fig. 30, the evolution of wave potential energy during wave breaking can be divided into three stages, corresponding to the time evolution of kinetic energy. In the energy dissipation stage, as wave breaking begins, the potential energy decreases over time. When the wave reaches the initial shoreline, the potential energy starts to increase. At the maximum run-up position of the wave, the potential energy reaches its peak. After reaching the maximum run-up and entering the energy conservation stage, the potential energy decreases again as the water flows back down the slope.

PFLBM can accurately simulate all three stages, whereas the increase in potential energy in FSLBM is less distinct. As discussed in Sec. V C 1, the kinetic energy in the single-phase flow model dissipates too rapidly, leaving insufficient kinetic energy to convert into potential energy. This shortfall affects the wave's ability to achieve a significant run-up after reaching the initial shoreline. It is important to note that the difference in dimensionless potential energy decrease between PFLBM and FSLBM arises from the differences in their computational domains.

Similarly, the time evolution of total energy during wave breaking is also divided into three stages in Fig. 31. During the energy dissipation stage, both kinetic and potential energy decrease over time, resulting in a continuous reduction of total energy. When the wave reaches the initial shoreline and begins to run up, kinetic energy decreases while potential energy increases. However, the rate of kinetic energy dissipation due to the entrainment of air greatly exceeds the increase in potential energy. This dissipation continues until the maximum run-up height is achieved, at which point the system transitions to the energy conservation stage and the kinetic energy is minimal, as illustrated in Fig. 29. At this stage, the total energy is predominantly composed of potential energy.

Throughout the energy dissipation stage, the kinetic energy dissipation is predominant. The FSLBM model exhibits faster kinetic energy dissipation compared to PFLBM, leading to a more rapid total energy dissipation in FSLBM. Figure 31 illustrates the difference in energy dissipation between two-phase and single-phase flows. Generally, the dissipation in kinetic energy of the water is primarily due to the dissipation of a substantial amount of energy through the interaction with the air phase during violent wave breaking. The presence of the air phase makes the energy dissipation in two-phase flow more accurate compared to single-phase flow.

In conclusion, during the energy dissipation stage, the potential energy of the water initially decreases and then increases until it reaches the maximum run-up height. However, because the rate of kinetic energy dissipation greatly exceeds the increase in potential energy, the total energy continues to decrease until this peak is reached. At this point, the system transitions to the energy conservation stage, where kinetic energy is minimal and the total energy is predominantly potential energy.

VI. CONCLUSIONS

In this study, a two-phase phase-field lattice Boltzmann model (PFLBM) is proposed to simulate the propagation and, especially, the breaking of solitary waves. The proper grid size, time step and interface thickness for the presented numerical model are selected via sensitivity analysis. The proposed method is validated through theoretical solutions and experimental results. Then, the transformation of a solitary wave over a slope is simulated, and the wave breaking phenomenon is investigated. The following conclusions can be obtained:

(1) Compared with those of the single-phase lattice Boltzmann model with a free surface, the numerical results of the phase-field lattice Boltzmann model for air–water two-phase flows agree better with the experimental measurements of solitary wave propagation over semicircular breakwater.
(2) PFLBM effectively simulates solitary wave breaking over a slope and provides detailed insights into three typical types of breakers—surging, plunging, and spilling—particularly in terms of air entrainment.
(3) When the solitary wave breaks, the air in front of the wave crest is pushed away from the wave front, forming a counterclockwise vortex. Another small clockwise-rotating vortex is generated below the large vortex, which shows that the mixture of air and water tends to roll into the water, revealing the flow structures of the plunging breaker caused by air entrainment.

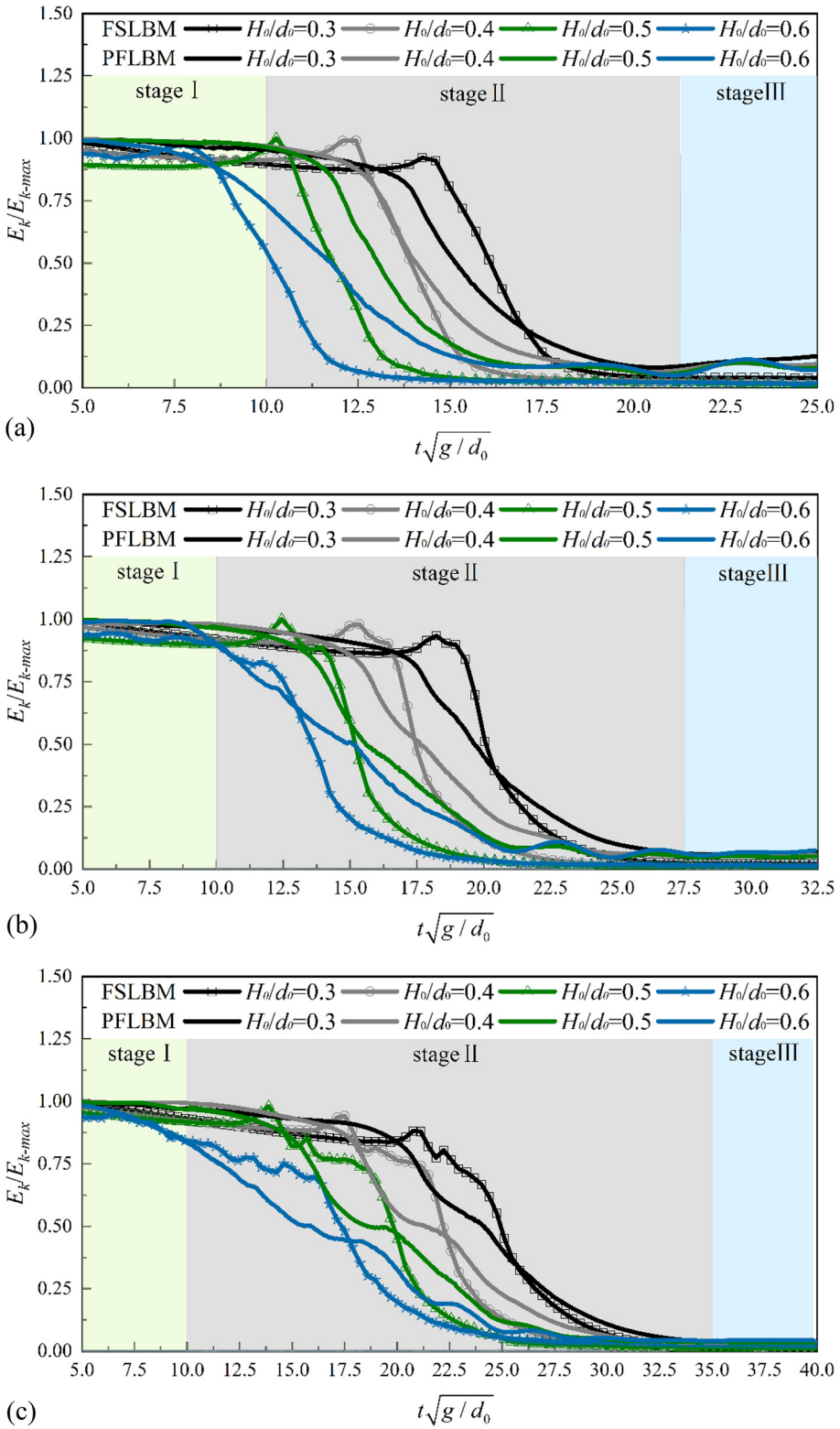

FIG. 28. The evolution of the kinetic energy of water for (a) s = 1/10, (b) s = 1/15, and (c) s = 1/20.

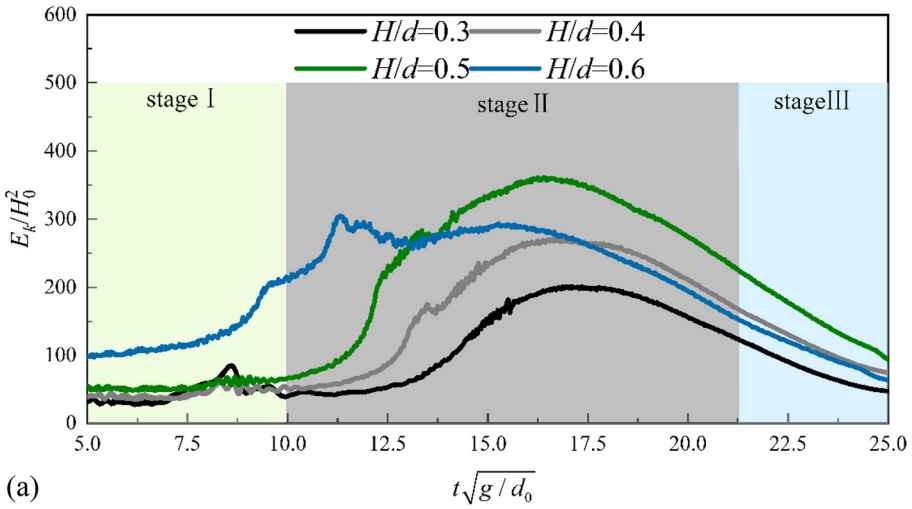

(a)

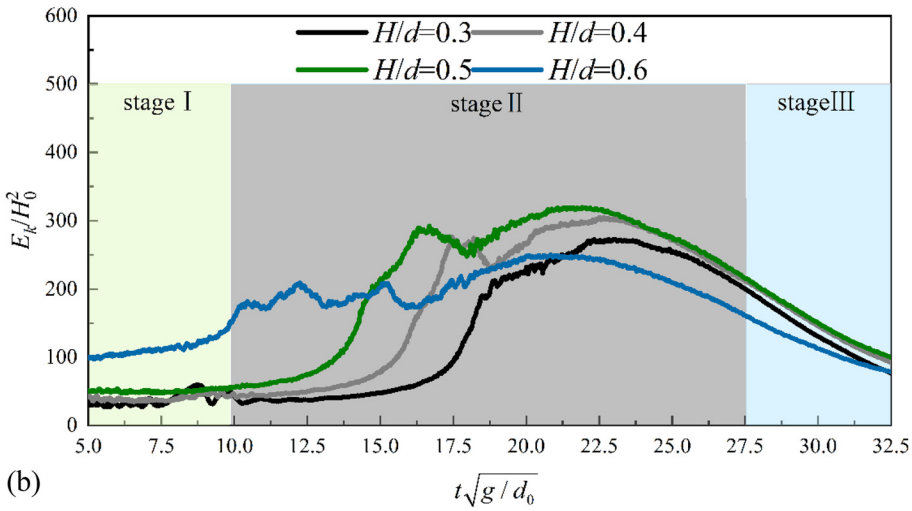

(b)

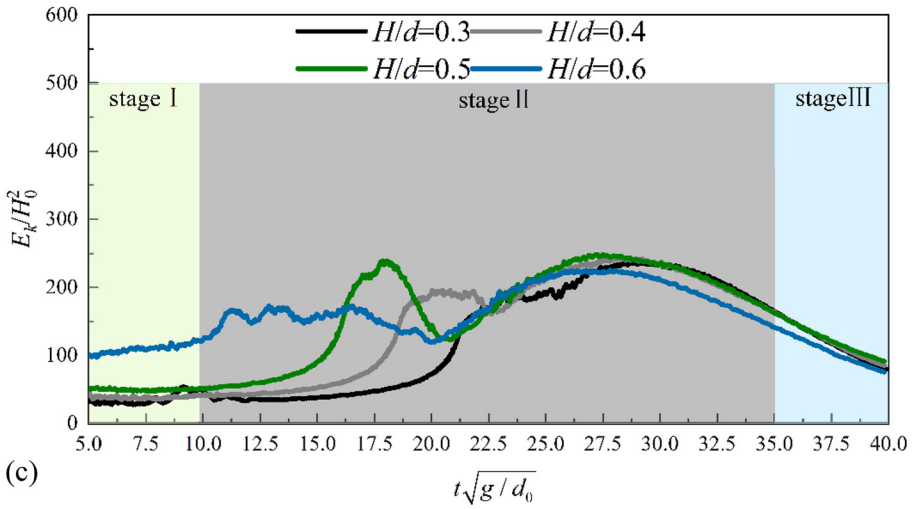

(c)

FIG. 29. The evolution of the air kinetic energy: (a) s = 1/10, (b) s = 1/15, and (c) s = 1/20.

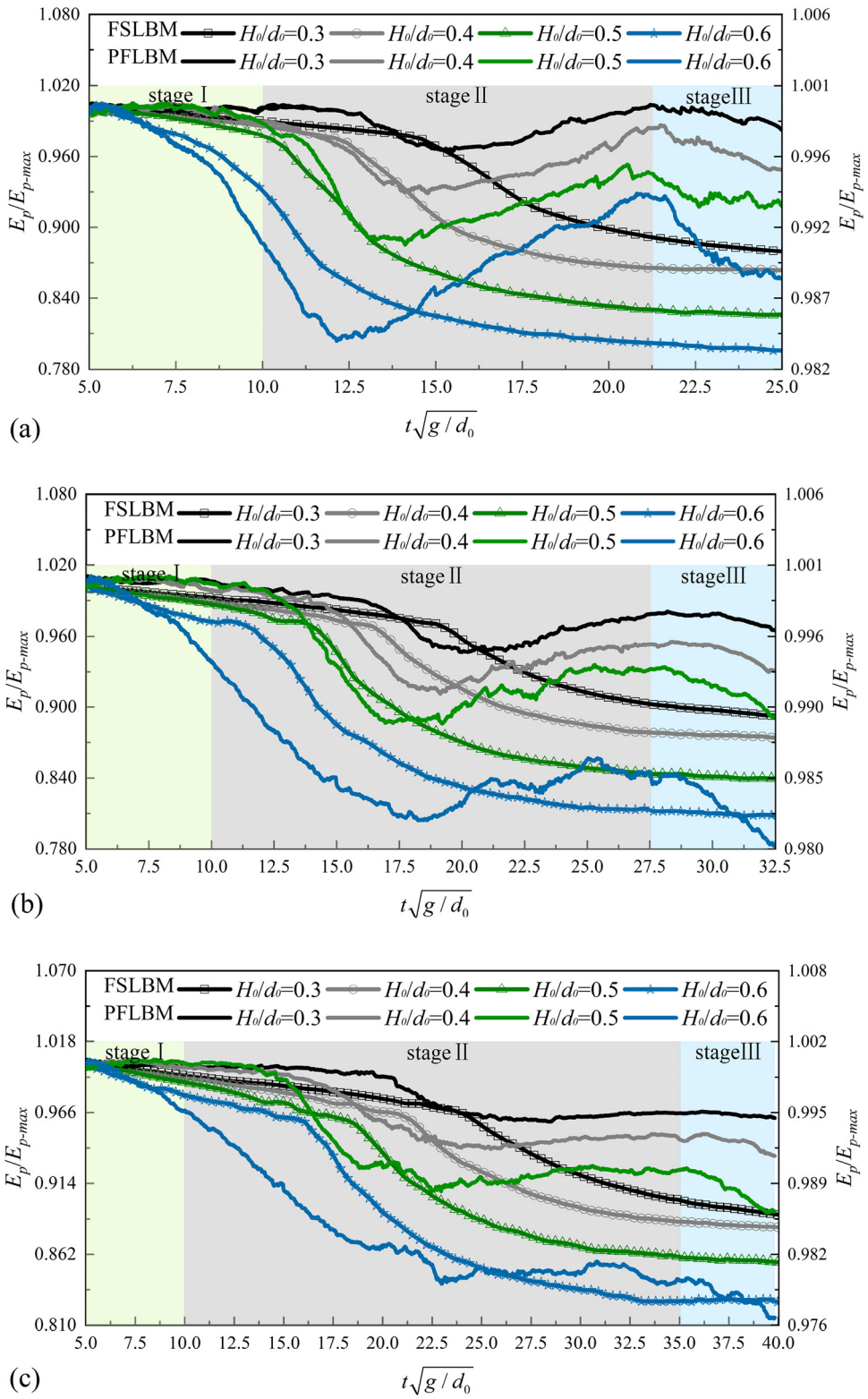

FIG. 30. The evolution of the potential energy of water for (a) s = 1/10, (b) s = 1/15, and (c) s = 1/20.

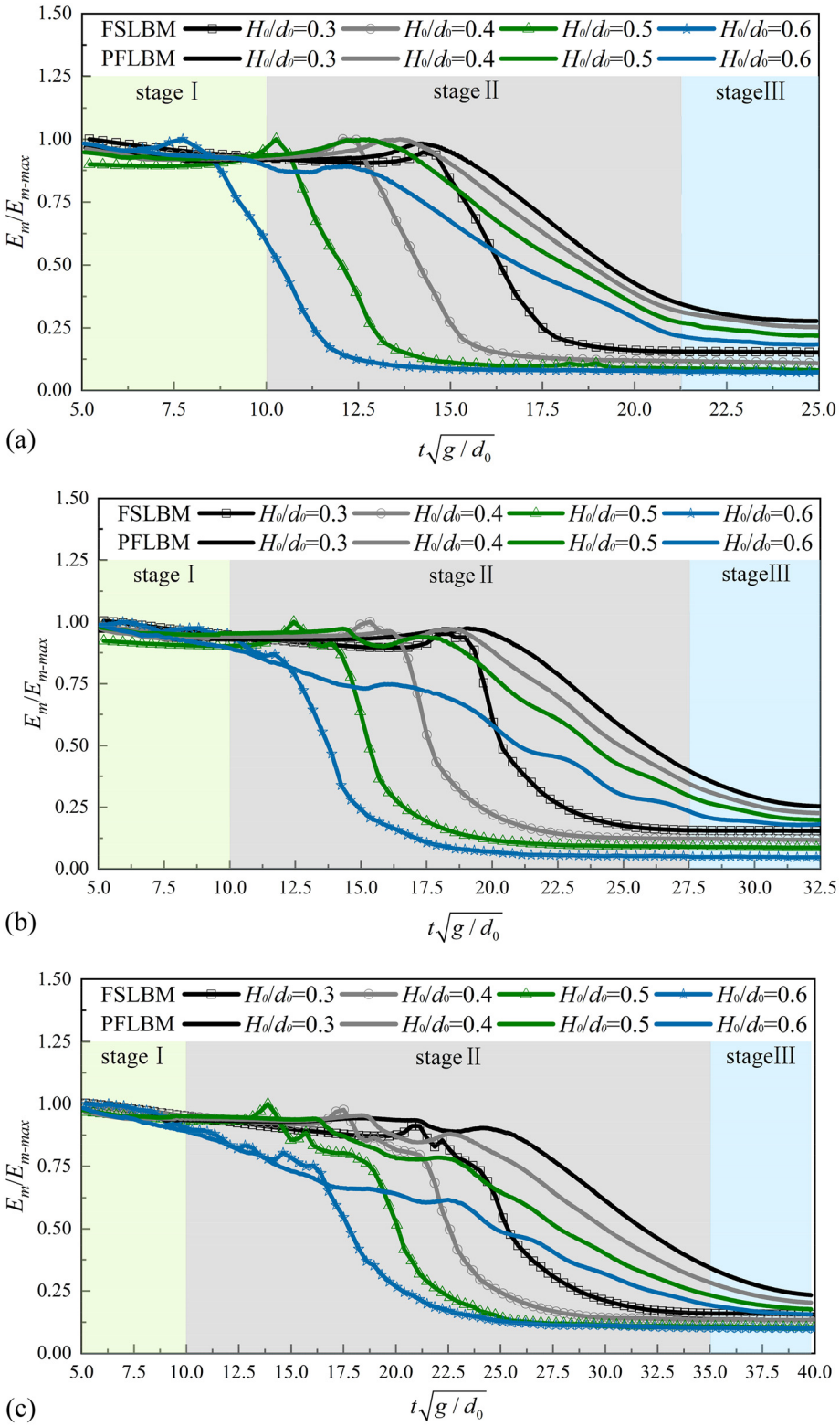

FIG. 31. The evolution of the total energy of water for (a) s = 1/10, (b) s = 1/15, and (c) s = 1/20.

(4) Air has been shown to play a crucial role in accurate simulations of breaking waves. Because of the existence of the air phase, it is more accurate to calculate the energy dissipation of water by two-phase flow than by single-phase flow. For the water phase, almost all the stages dissipate kinetic energy until the maximum run-up is reached; then, the kinetic energy is very small. The air phase absorbs kinetic energy from water as the wave breaks and dissipates kinetic energy after the maximum run-up is reached.
(5) During the energy dissipation stage, the water's potential energy first decreases, then increases until it reaches the maximum run-up height. However, because the rate of kinetic energy dissipation significantly exceeds the increase in potential energy, the total energy continues to decrease until this peak is achieved. At this point, the system transitions to the energy conservation stage, where kinetic energy is minimal and the total energy is primarily potential energy.

ACKNOWLEDGMENTS

This study was financially supported by the National Key Research and Development Program of China (Grant No. 2021YFB2601100) and the National Natural Science Foundation of China (Grant No. 52301335).

AUTHOR DECLARATIONS

Conflict of Interest

The authors have no conflicts to disclose.

Author Contributions

Jiahe Zhou: Conceptualization (lead); Data curation (lead); Formal analysis (lead); Investigation (lead); Methodology (lead); Software (lead); Validation (lead); Visualization (lead); Writing – original draft (lead); Writing – review & editing (lead). **Qinghe Zhang:** Conceptualization (supporting); Data curation (supporting); Methodology (supporting); Supervision (supporting); Writing – review & editing (supporting). **Guangwei Liu:** Conceptualization (supporting); Funding acquisition (supporting); Investigation (supporting); Methodology (supporting); Software (supporting); Supervision (supporting); Writing – review & editing (supporting). **Jinfeng Zhang:** Funding acquisition (lead); Resources (supporting); Supervision (supporting); Writing – review & editing (supporting). **Enbo Xing:** Formal analysis (supporting); Investigation (supporting); Methodology (supporting); Software (supporting).

DATA AVAILABILITY

The data that support the findings of this study are available from the corresponding author upon reasonable request.

REFERENCES

[1]C. E. Synolakis, "The runup of long waves," Ph.D. thesis (California Institute of Technology, 1986).
[2]Y. Li, *Tsunamis: Non-Breaking and Breaking Solitary Wave Run-up* (California Institute of Technology, 2000).
[3]Y. Li and F. Raichlen, "Solitary wave runup on plane slopes," J. Waterw., Port, Coastal, Ocean Eng. **127**(1), 33–44 (2001).
[4]A. Jensen, S. Mayer, and G. K. Pedersen, "Experiments and computation of onshore breaking solitary waves," Meas. Sci. Technol. **16**(10), 1913 (2005).
[5]S.-C. Hsiao *et al.*, "On the evolution and run-up of breaking solitary waves on a mild sloping beach," Coastal Eng. **55**(12), 975–988 (2008).
[6]Y.-T. Wu *et al.*, "Runup of laboratory-generated breaking solitary and periodic waves on a uniform slope," J. Waterw., Port, Coastal, Ocean Eng. **144**(6), 04018023 (2018).
[7]H.-Y. Lo, Y. S. Park, and P. L.-F. Liu, "On the run-up and back-wash processes of single and double solitary waves—An experimental study," Coastal Eng. **80**, 1–14 (2013).
[8]H. J. Hafsteinsson, F. M. Evers, and W. H. Hager, "Solitary wave run-up: Wave breaking and bore propagation," J. Hydraul. Res. **55**(6), 787–798 (2017).
[9]Y. Li and F. Raichlen, "Non-breaking and breaking solitary wave run-up," J. Fluid Mech. **456**, 295–318 (2002).
[10]J. A. Zelt, "The run-up of nonbreaking and breaking solitary waves," Coastal Eng. **15**(3), 205–246 (1991).
[11]P. K. Stansby, "Solitary wave run up and overtopping by a semi-implicit finite-volume shallow-water Boussinesq model," J. Hydraul. Res. **41**(6), 639–647 (2003).
[12]A. G. L. Borthwick *et al.*, "Solitary wave transformation, breaking and run-up at a beach," Proc. Inst. Civ. Eng.: Marit. Eng. **159**(3), 97–105 (2006).
[13]Y. V. Kartashov, B. A. Malomed, and L. Torner, "Solitons in nonlinear lattices," Rev. Mod. Phys. **83**(1), 247 (2011).
[14]B. Guo, L. Ling, and Q. P. Liu, "Nonlinear Schrödinger equation: Generalized Darboux transformation and rogue wave solutions," Phys. Rev. E **85**(2), 026607 (2012).
[15]P. G. Chamberlain and D. Porter, "The modified mild-slope equation," J. Fluid Mech. **291**, 393–407 (1995).
[16]L. H. Holthuijsen, A. Herman, and N. Booij, "Phase-decoupled refraction–diffraction for spectral wave models," Coastal Eng. **49**(4), 291–305 (2003).
[17]S. E. Harris and D. G. Crighton, "Solitons, solitary waves, and voidage disturbances in gas-fluidized beds," J. Fluid Mech. **266**, 243–276 (1994).
[18]T. J. Bridges, "A universal form for the emergence of the Korteweg–de Vries equation," Proc. R. Soc. A **469**(2153), 20120707 (2013).
[19]F. He, Y. Zhang, H. Jiang *et al.*, "Numerical investigation of solitary wave breaking over a slope based on multi-phase smoothed particle hydrodynamics," Phys. Fluids **35**(2), 023313 (2023).
[20]P. Lin, K.-A. Chang, and P. L.-F. Liu, "Runup and rundown of solitary waves on sloping beaches," J. Waterw., Port, Coastal, Ocean Eng. **125**(5), 247–255 (1999).
[21]D. Liang *et al.*, "Boussinesq modelling of solitary wave and N-wave runup on coast," Appl. Ocean Res. **42**, 144–154 (2013).
[22]S. T. Grilli, I. A. Svendsen, and R. Subramanya, "Breaking criterion and characteristics for solitary waves on slopes," J. Waterw., Port, Coastal, Ocean Eng. **123**(3), 102–112 (1997).
[23]Z. Xie and T. Stoesser, "Two-phase flow simulation of breaking solitary waves over surface-piercing and submerged conical structures," Ocean Eng. **213**, 107679 (2020).
[24]R. Cienfuegos, E. Barthélemy, and P. Bonneton, "Wave-breaking model for Boussinesq-type equations including roller effects in the mass conservation equation," J. Waterw., Port, Coastal, Ocean Eng. **136**(1), 10–26 (2010).
[25]T. Sakakiyama and R. Kajima, "Numerical simulation of nonlinear wave interacting with permeable breakwaters," in *Proceedings of Coastal Engineering 1992* (ASCE, 1993), pp. 1517–1530.
[26]T. Nakayama and M. Mori, "An Eulerian finite element method for time-dependent free surface problems in hydrodynamics," Int. J. Numer. Methods Fluids **22**(3), 175–194 (1996).
[27]M. Garzon and J. A. Sethian, "Wave breaking over sloping beaches using a coupled boundary integral-level set method," in *Free Boundary Problems, International Series of Numerical Mathematics* (Birkhäuser Basel, 2006).
[28]P. Lin and P. L.-F. Liu, "A numerical study of breaking waves in the surf zone," J. Fluid Mech. **359**, 239–264 (1998).
[29]Y. Watanabe, H. Saeki, and R. J. Hosking, "Three-dimensional vortex structures under breaking waves," J. Fluid Mech. **545**, 291–328 (2005).
[30]D. Wang and P. L.-F. Liu, "An ISPH with modified k–ε closure for simulating breaking periodic waves," Coastal Eng. **178**, 104191 (2022).
[31]C. Tsurudome *et al.*, "Study of beach permeability's influence on solitary wave runup with ISPH method," Appl. Ocean Res. **117**, 102957 (2021).

[32]A. Khayyer, H. Gotoh, and S. D. Shao, "Corrected incompressible SPH method for accurate water-surface tracking in breaking waves," Coastal Eng. **55**(3), 236–250 (2008).
[33]F. He and H. Zhang *et al.*, "Numerical investigation of the solitary wave breaking over a slope by using the finite particle method," Coastal Eng. **156**, 103617 (2020).
[34]X. Guo and B. D. Rogers *et al.*, "New massively parallel scheme for incompressible smoothed particle hydrodynamics (ISPH) for highly nonlinear and distorted flow," Comput. Phys. Commun. **233**, 16–28 (2018).
[35]J. D. Sterling and S. Chen, "Stability analysis of lattice Boltzmann methods," J. Comput. Phys. **123**(1), 196–206 (1996).
[36]T. Pohl *et al.*, "Optimization and profiling of the cache performance of parallel lattice Boltzmann codes," Parallel Process. Lett. **13**(04), 549–560 (2003).
[37]S. Williams and J. Carter *et al.*, "Optimization of a lattice Boltzmann computation on state-of-the-art multicore platforms," J. Parallel Distrib. Comput. **69**(9), 762–777 (2009).
[38]S. Habibah Shafiai, "Lattice Boltzmann method for simulating shallow free surface flows involving wetting and drying," Ph.D. thesis (University of Liverpool, 2011).
[39]S. H. Shafiai, "A lattice Boltzmann model for the 2D solitary wave run-up around a conical island," *From Sea to Shore–Meeting the Challenges of the Sea: Coasts, Marine Structures and Breakwaters 2013* (ICE Publishing, 2014).
[40]C. F. Janssen, M. Krafczyk, and S. T. Grilli, "Modeling of wave breaking and wave-structure interactions by coupling of fully nonlinear potential flow and lattice-Boltzmann models," in ISOPE International Ocean and Polar Engineering Conference (ISOPE), 2010.
[41]G. Liu, J. Zhang, and Q. Zhang, "A high-performance three-dimensional lattice Boltzmann solver for water waves with free surface capturing," Coastal Eng. **165**, 103865 (2021).
[42]P. D. Hieu and K. Tanimoto, "Verification of a VOF-based two-phase flow model for wave breaking and wave–structure interactions," Ocean Eng. **33**(11–12), 1565–1588 (2006).
[43]C. Schwarzmeier *et al.*, "Comparison of free-surface and conservative Allen–Cahn phase-field lattice Boltzmann method," J. Comput. Phys. **473**, 111753 (2023).
[44]A. Babanin, *Breaking and Dissipation of Ocean Surface Waves* (Cambridge University Press, 2011).
[45]Z. Wang, J. Yang, and F. Stern, "High-fidelity simulations of bubble, droplet and spray formation in breaking waves," J. Fluid Mech. **792**, 307–327 (2016).
[46]A. Fakhari and T. Mitchell *et al.*, "Improved locality of the phase-field lattice-Boltzmann model for immiscible fluids at high density ratios," Phys. Rev. E **96**(5), 053301 (2017).
[47]G. Gruszczyński and T. R. Mitchell *et al.*, "A cascaded phase-field lattice Boltzmann model for the simulation of incompressible, immiscible fluids with high density contrast," Comput. Math. Appl. **79**(4), 1049–1071 (2020).
[48]Y. P. Sitompul and T. Aoki, "A filtered cumulant lattice Boltzmann method for violent two-phase flows," J. Comput. Phys. **390**, 93–120 (2019).
[49]P.-H. Chiu and Y.-T. Lin, "A conservative phase field method for solving incompressible two-phase flows," J. Comput. Phys. **230**(1), 185–204 (2011).
[50]I. A. Svendsen, *Introduction to Nearshore Hydrodynamics* (World Scientific Publishing Company, 2005), p. 744.
[51]X. Han and S. Dong, "Interaction of solitary wave with submerged breakwater by smoothed particle hydrodynamics," Ocean Eng. **216**, 108108 (2020).
[52]M. J. Cooker and D. H. Peregrine *et al.*, "The interaction between a solitary wave and a submerged semicircular cylinder," J. Fluid Mech. **215**, 1–22 (1990).
[53]Z. Yang, B.-Q. Deng, and L. Shen, "Direct numerical simulation of wind turbulence over breaking waves," J. Fluid Mech. **850**, 120–155 (2018).
[54]T. Mitchell, C. Leonardi, and A. Fakhari, "Development of a three-dimensional phase-field lattice Boltzmann method for the study of immiscible fluids at high density ratios," Int. J. Multiphase Flow **107**, 1–15 (2018).
[55]T. Krüger *et al.*, *The Lattice Boltzmann Method* (Springer International Publishing, 2017), pp. 4–15.
[56]Q. Dahong, "The application of Cnoidal wave theory," J. Dalian Univ. Technol. **21**(1), 87–96 (1982) (in Chinese).
[57]M.-O. Bristeau, A. Mangeney, J. Sainte-Marie, and N. Seguin, "An energy-consistent depth-averaged Euler system: Derivation and properties," Discrete Contin. Dyn. Syst. - B **20**(4), 961–988 (2015).